Upslope Sediment Transport on Continental Margins: A Process-Oriented Numerical Study

J. Kämpf[1]

[1]College of Science and Engineering, Flinders University, Adelaide, Australia.

Corresponding author: Jochen Kaempf (jochen.kaempf@flinders.edu.au)

Key Points:

- Explores the dispersal of particles in stratified flows on continental slopes
- Interaction of slope currents with submarine channels can facilitate a diapycnal upslope flux of particles
- Sediment settling enhances this upslope flux of particles

Abstract

Using the method of process-oriented hydrodynamic modelling, this work investigates the dispersal of particles in stratified fluids on continental margins. The focus is placed on steady-state density distributions that are governed by an advective-diffusive balance. In this case, particles can still be advected across isopycnal surfaces, given that turbulent fluctuations do generally not offset the advective displacement of a particle. The validity of this fundamental principle is demonstrated here with the diapycnal upslope sediment transport in a bottom Ekman layer that forms under a stratified geostrophic slope current. Similarly, this study demonstrates that interaction between slope currents with a submarine channel can facilitate a continuous diapycnal upslope flux of particles, confined to the lowermost 10-20 m of the water column. Velocity anomalies that facilitate this upslope sediment flux are the signature of standing topographic Rossby waves, that can only develop for slope currents that are left-bounded (right-bounded) by shallower water in the northern (southern) hemisphere. Findings of sensitivity studies confirm the existence of up-channel flows for a wide range of parameter values. Under the assumption that particles remain suspended in the water column, the inclusion of gravitational settling significantly increases the up-channel sediment flux. Sediment settling operates to trap particles close to the seafloor within the core of bottom-intensified up-channel flow. The author postulates that this mechanism plays an important role in biogeochemical cycles at continental margins.

Plain Language Summary

Continental margins are replete with submarine canyons and channels. Some but not all canyons underpin productive and diverse marine habitats, for scientific reasons yet to be discovered. Previous research suggests that canyons are the downward conduits of sediment in turbidity currents. However, recent deep observations inside the Whittard Canyon (NE Atlantic) provided evidence of continuous up-canyon currents that, modulated by tides, trigger upslope sediment transport in the upper 2500 m of the canyon. This study provides a possible theoretical explanation of this observational evidence. Here we show that canyon-flow interaction induces a concentrated and bottom-intensified up-channel current. While this current does not significantly disturb the ambient density field, which is governed by an advective-diffusive balance, it is an agent of continuous upslope sediment transport. This process constitutes a yet largely unexplored return path of particulate (organic and inorganic) matter at continental margins.

1 Introduction

Particulate matter plays an important role in geomorphological and biogeochemical cycles in the oceans. For instance, it underpins an elusive branch of marine food webs that is based on suspension feeding (e.g., Hentschel and Shimeta, 2008). The dynamics and transport of particulate matter at continental margins has been intensively studied both in the field and theoretically in the past. Submarine canyons and channels are the key transport routes of suspended sediment particles. Their presence creates complex oceanic flows that locally enhance primary productivity and increase particulate matter concentrations (e.g., Bosley *et al.*, 2004).

Puig *et al.* (2014) provide a detailed review of sediment-transport processes in submarine canyons, dominated by storm-induced turbidity currents and dense shelf-water cascading (e.g., Wåhlin, 2002), failures of recently deposited fluvial sediments, canyon-flank failures, and trawling-induced resuspension. These transport processes commonly deposit sediments in the upper and middle reaches of canyons for decades or centuries before being completely or partially flushed farther down-canyon by large sediment failures. Additionally, the review concludes that internal waves (e.g., Hotchkiss and Wunsch, 1982; Kunze *et al.*, 2002) periodically resuspend ephemeral deposits within canyons and contribute to dispersing particles or retaining and accumulating them in specific regions. On the other hand, submarine canyons often trap tidal energy and strongly amplify tidal flows (Cacchione *et al.*, 2002; Vlasenko *et al.*, 2016; Alberty *et al.*, 2017; Nazarian and Legg, 2017a,b); Waterhouse *et al.*, 2017) and thereby facilitate the erosion and transport of sediment (e.g. Cacchione *et al.*, 2002).

Allen and Durrieu de Madron (2009) reviewed scientific knowledge of the role that shelf-incising canyons in the exchange of water masses including particulate matter across the shelf break. They conclude that such shelf-break canyons are often regions of the generation of strong baroclinic tides and internal waves leading to greatly elevated levels of mixing. Previous canyon studies (Freeland and Denman, 1982; Klinck, 1996; Hickey, 1997; Allen *et al.*, 2001; Kämpf, 2006) suggested that, in the northern (southern) hemisphere, left-bounded (right-bounded) slope currents can trigger swift up-canyon flows. Theoretical considerations by Kämpf (2012; 2018) revealed that the up-canyon flows are the signature of stationary (standing) topographic Rossby waves, whose generation is direction-dependent. It should be highlighted that most previous studies on shelf-break canyons focused on the upwelling of dissolved and not particulate substances, which can be substantial different, as demonstrated here. While the dynamics in and around shelf-break canyons is relatively well researched, less is known about processes at much greater depths of deep-sea canyons.

Most previous studies infer a predominantly downslope sediment flux at continental margins, which is not surprising given the negative buoyancy of sediment particles. However, a few recent studies report the existence of up-channel sediment fluxes. Puig *et al.* (2003) studied the sediment transport in the bottom boundary layer at a depth of 276 m near the head of the West Halibut Canyon off Newfoundland during winter 2008–2009. They identified short events of sporadic bottom intensified up-canyon flows (~40 cm s^{-1}) that triggered transient peaks in

suspended sediment concentrations, lasting less than an hour. Puig *et al.* (2003) interpreted these peaks as the up-canyon propagation of semidiurnal internal tidal bores carrying fine sediment particles resuspended from deeper canyon regions. On the other hand, Amaro *et al.* (2015; 2016) reported deep observations reported from the Whittard Canyon (NE Atlantic), where several near-bottom deployments measuring currents, temperature, salinity, turbidity and sediment flux were carried out between 2007 and 2012, lasting from a few days up to an entire year. These deployments extended from the shelf edge to greater depths of up to 4166 m in a deep-sea channel. The observations confirmed that the near-bed current regime in the upper canyon reaches (from the shelf edge to about 2500 m depth) is dominated by moderate to strong semi-diurnal tidal currents. In the lower reaches of the canyon, tidal currents appeared weaker, not exceeding 0.1-0.15 m s^{-1} and with no sign of resuspension of bottom sediment (Amaro *et al.*, 2015). Surprisingly, however, during most of the 1-year deployment period, the net near-bottom currents were generally directed in an up-canyon direction throughout the canyon. Hence, assisted by intensified tidal currents, the net near-bottom currents induced a persistent up-canyon transport of suspended particulate matter in the upper canyon reaches. The ultimate cause of this upslope sediment transport is unknown.

This work is based on the fundamental feature that particles can move relative to an arrested density field governed by a balance between advective effects due to currents and diffusive effects due to turbulence. In this situation, the same currents that no longer modify the density field can still move particles across density surfaces, given that, on average, turbulent fluctuations only modify but not offset the advective particle displacements. One prominent example of such persistent diapycnal movement of particles is the trapping of suspended sediment within high-turbidity regions in positive estuaries (e.g. Yu *et al.*, 2015). It should be highlighted that Kunze *et al.* (2012) have employed an advective–diffusive balance to interfere turbulence-driven flows in submarine canyons; and they derive horizontal upslope flows of 10–50 m day^{-1} for the Monterey and Soquel Submarine Canyons (located offshore of central California). The present study demonstrates that the advective–diffusive balance also underpins current-induced upslope flows of much greater speeds of 0.1-0.2 m/s (8-16 km day^{-1}).

2 Methods

2.1 Model description

This study applies the hydrodynamic model COHERENS (Luyten *et al.*, 1999). The governing equations are the finite-difference forms of conservation equations for momentum, heat, volume and scalars for an incompressible fluid on the *f* plane cast in terrain-following sigma coordinates. COHERENS is based on the same physical laws and coordinate transformation and similar numerical algorithms that govern other sigma coordinate models such as POM (Blumberg and Mellor, 1987) or ROMS (Shchepetkin and McWilliams, 2005). The Coriolis parameter in the control experiment is set to $f = -1\times10^{-4}$ s^{-1}, corresponding to a

geographical latitude of 45°S. Results are readily transferable to the northern hemisphere simulation. In this process-oriented application, temperature effects are ignored, and the density of seawater, ρ, is exclusively related to salinity, S, via a linear equation of state:

$$\rho(S) = \rho_o[1 + \beta(S - S_o)] \quad (1)$$

where ρ_o = 1026 kg/m^3, $\beta = 7.6\times10^{-4}$ and S_o = 34 (no units). In the original model formulation, the buoyancy force is calculated with reference to the initial density distribution. This can trigger the creation of unwanted currents due to the initial coordinate adjustment of the density field. In this application, horizontal gradients of the buoyancy force are calculated with reference to their initial values. This technique eliminates such adjustment problems.

Turbulent Prandtl numbers of unity are assumed for both horizontal ($A_h = D_h$) and vertical ($A_z = D_z$) diffusion. For the ease of interpretation, most experiments discussed here employ constant values of A_h = 1 m^2 s^{-1} and A_z = 0.02 m^2 s^{-1}. The latter corresponds to a vertical scale of the bottom Ekman layer of $\delta_E = \sqrt{2A_z/|f|} \approx$ 20 m. The use of the k-ε turbulence closure for A_z and/or the Smagorinsky turbulence scheme for A_h yielded qualitatively similar results (not shown). A quadratic bottom-friction parameterization is employed. The associated bottom friction coefficient, c_D, can be related to a roughness length, δ, via the relationship (see Luyten *et al.*, 1999):

$$c_D = [\ln(z^*/\delta)/\kappa]^{-2} \quad (2)$$

where z^* is the distance between the horizontal velocity grid point and the seafloor and κ = 0.4 is the von Kármán constant.

COHERENS includes a sophisticated Lagrangian particle tracking module, in which the gridded velocity field is interpolated to the particle location to calculate particle movements from accurate logarithmic displacement laws (see Luyten *et al.*, 1999). The associated maximum turbulent velocity components can be calculated from (Maier-Reimer, 1980):

$$(u^T_{\max}, v^T_{\max}, w^T_{\max}) = \sqrt{6(D_h, D_h, D_z)/\Delta t} \quad (3)$$

where Δt is the numerical time step. The turbulent velocities are then determined for each particle with the Monte-Carlo method which consists in multiplying each maximum current component by a random generated number between -1 and 1. These diffusive velocity components are then added to the advective velocity components before the calculation of particle displacements. With Δt = 60 s, relation (3) implies maximum horizontal and vertical turbulent velocities of ~0.32 m s^{-1} and 0.02 m s^{-1}, respectively. This velocity can displace a particle horizontally at maximum by ~19 m and vertically by 1.2 m during a timestep. The author also added a settling velocity, w_s, to simulate the negative buoyancy of particles. Only the upper range of observed settling velocities, w_s = 1-5 mm s^{-1}, (see McDonnell and Buesseler, 2010) is

159 considered here. For simplicity, interactions with the seafloor (i.e. erosion or deposition) are
160 ignored. It is also assumed that suspended particles do not influence the fluids' density.

161

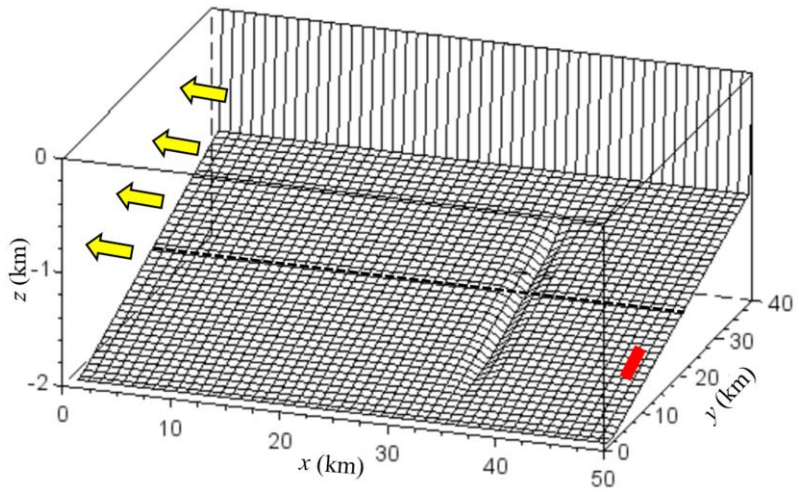

162

163 **Figure 1:** Model bathymetry for experiment A (see Fig. 2a). Arrows indicate the direction of the
164 ambient geostrophic flow. The red line indicates the deployment region of Lagrangian floats.

165

166 2.2 Experimental design

167 The model region is 50 km long and 40 km wide, resolved by an equidistant horizontal
168 grid spacing of $\Delta x = \Delta y = 1$ km (**Figure 1**). A total of 60 vertical sigma levels are used. The
169 lowermost 25 levels are kept at a fine vertical spacing of 2 m to adequately resolve the structure
170 of the bottom Ekman layer. The simplified continental margin has a constant bottom slope with
171 isobaths running parallel to the *x*-axis. In most experiments, total water depth varies from 2 km
172 along the deeper boundary of the domain to 1 km on the opposite side, corresponding to a bottom
173 inclination of 0.025 (1.43^{o} slope). The shallower boundary is treated as a nonpermeable coast.
174 Zero-gradient conditions are used at the open lateral boundaries. The sea level along the offshore
175 boundary is kept at its initial value (zero elevation).

176 A single submarine channel is embedded in the continental slope. Its axis runs
177 perpendicular to the ambient isobaths. The channel vanishes in both shallower and deeper water
178 to avoid any dynamical disturbances near boundaries. A variety of channel geometries are
179 considered in a range of experiments with channel depths, *H*, ranging between 50 and 200 m and
180 channel widths, *W*, ranging between 3 and 10 km (**Figure 2a**). Additional experiments consider
181 U-shaped and V-shaped channel configurations (**Figure 2b**).

182

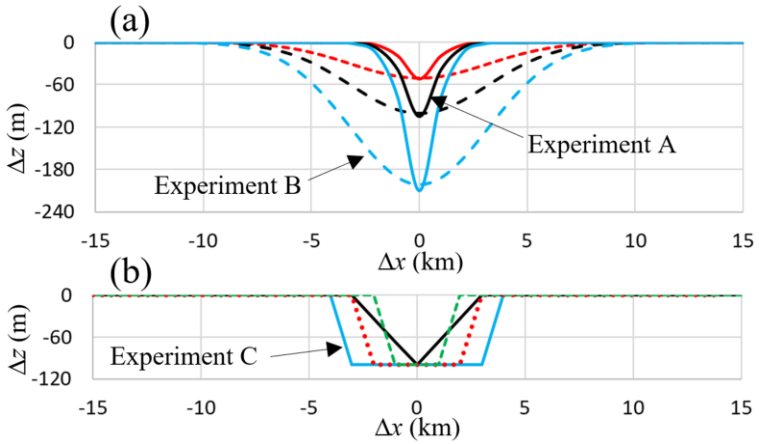

Figure 2: Different shapes of submarine channels considered in a sequence of model runs. Here Δx denotes the distance from the channel axis, and Δz the bathymetry relative to the ambient seafloor. Experiments A, B and C denote configurations of experiments that are discussed in detail in the text.

Each experiment commences with a constant vertical salinity gradient. In the control experiment, this gradient is 0.001 m^{-1}, i.e. a increase of one salinity unity per km depth. This corresponds to a value of the stability frequency, N, of ~2.2×10^{-3} s^{-1}, which reflects a typical situation. The stability frequency is calculated from $N^2 = -g/\rho_o \partial\rho/\partial z$, where g = 9.81 m/s^2 is acceleration due to gravity and z is the vertical coordinate.

With a constant horizontal and vertical grid spacing near the seafloor, the salinity conservation equation in sigma coordinates is equivalent to its Cartesian form; that is,

$$\frac{\partial S}{\partial t} = -\left(u\frac{\partial S}{\partial x} + v\frac{\partial S}{\partial y} + w\frac{\partial S}{\partial z}\right) + D_h\left(\frac{\partial^2 S}{\partial x^2} + \frac{\partial^2 S}{\partial y^2}\right) + D_z\frac{\partial^2 S}{\partial z^2} \quad . \qquad (4)$$

The horizontal velocity (u, v) can then be interpreted as the bottom-parallel velocity, and the corresponding vertical coordinate z is oriented perpendicular to the seafloor. Equation (4) is used to analyze the resultant steady-state salinity fields.

The total simulation time of experiments is 10 days, using external and internal numerical time steps of 3 s and 60 s, respectively. Each experiment is forced by the prescription of an along-slope barotropic pressure-gradient force in the first 5 grid cells adjacent to the downstream boundary. This forcing, which is implemented in the depth-integrated momentum equations of the model, operates to create a cross-slope barotropic pressure gradient in the entire model domain driving a geostrophic along-slope flow. The magnitude of this forcing is adjusted and varied such that the target speed of the slope current is reached within 2 days of simulation. In the control experiment, the speed of this slope current is set to 20 cm s^{-1} to reflect the features of the Flinders Current found on Australia's southern continental margin (Middleton and Bye, 2007). Sensitivity experiments consider weaker slope currents of speeds as low as 5 cm s^{-1}. The

slope current created is directed opposite to the phase propagation direction of free topographic Rossby waves that have shallower water on their left in the southern hemisphere. This situation supports the formation of standing topographic Rossby waves that are instrumental in cross-shelf exchanges induced by shelf-break canyons (see Kämpf, 2012; 2018).

Table 1: Parameter settings and variations

Parameter	Symbol	Unit	Control value	Variations
Ambient flow speed	U	cm/s	20	5, 10
Channel width[a]	W	km	5	10
Channel depth[a]	H	m	100	0, 50, 200
Stability frequency	N	10^{-3} s^{-1}	2.17	0.86, 1.91, 3.82
Coriolis parameter	f	10^{-4} s^{-1}	-1.0	-0.8, -1.2, -1.4
Vertical eddy diffusivity	D_Z	10^{-2} m^2/s	2.0	0.02, 0.2, 0.5, 5.0
Horizontal eddy diffusivity	D_H	m^2/s	1.0	5.0, 10.0
Bed roughness length	δ	mm	2.0	0.2, 10.0
Bottom drag coefficient[b]	C_D	10^{-3}	4.3	2.3, 7.9
Ambient bottom inclination	s	m/km	25 (≈1.4^o)	17.5, 32.5 (1^o-1.9^o)

[a]Additional experiments consider U-shape and V-shape channels (see Figure 2b).

[b]Value corresponding to δ, calculated from (2).

After an initial adjustment phase of two days, a total of 2000 neutrally buoyant particles are gradually released upstream from the lower portion of the submarine channel within a random distance of up to 50 m from the seafloor. Particles are hereby released at a random horizontal location along the red line shown in Figure 1 at a rate of 17 particles per hour over a time interval of 5 days. Total water depth along the deployment line varies between 1750 and 1875 m. Since the slope current is relatively uniform upstream from the canyon, the results are invariant on variations of the deployment location of particles. For the sake of comparison, particles reaching water depths <1500 m by the end of the simulation are defined as “upwelled” particles.

Table 1 summarizes the parameter settings for experiment A and another 40 sensitivity experiments. The parameter variations correspond to ranges of the canyon Rossby number, $Ro = U/(W|f|)$, between 0.16 and 0.83, the canyon Froude number, $Fr = U/(NH)$, between 0.1 and 4.6, and the canyon Burger number, $Bu = (Ro/Fr)^2$ between 0.02 and 3.3. In addition, the thickness of the bottom Ekman layer, $\delta_E = \sqrt{2A_z/|f|}$, is varied between 10 and 32 m. In additional model runs, the sign of the Coriolis parameter is reversed to $f = 1\times10^{-4}$ s^{-1} (northern hemisphere) such that the slope current is aligned with the direction of free topographic Rossby waves. In this case, the forcing is applied near the right-hand boundary, such that initial Rossby-wave disturbances travel away from it. As shown by the results, this configuration suppresses the creation of up-channel flows.

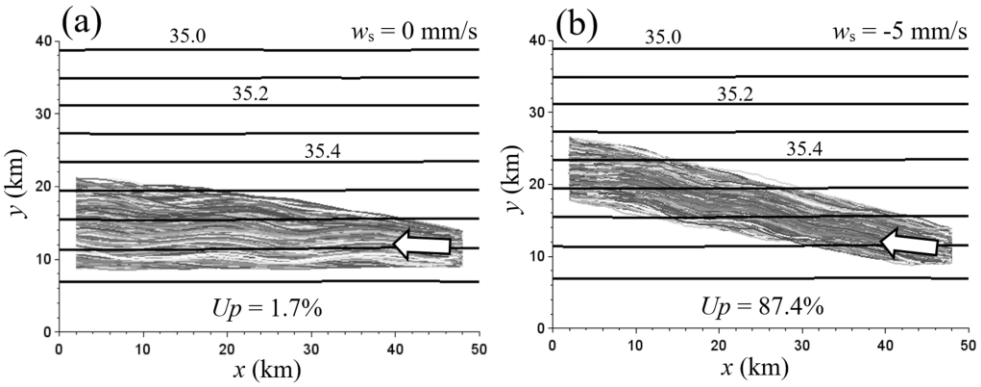

Figure 3: No-channel experiment. Trajectories of 2000 particles with a settling speed of a) w_s = 0 mm s^{-1} and b) w_s = -5 mm s^{-1}. The lines are steady-state isohalines of the salinity field in the bottom-nearest model layer. "Up" refers to the percentage of particles that reach a water depth >1500 m after 10 days of simulation.

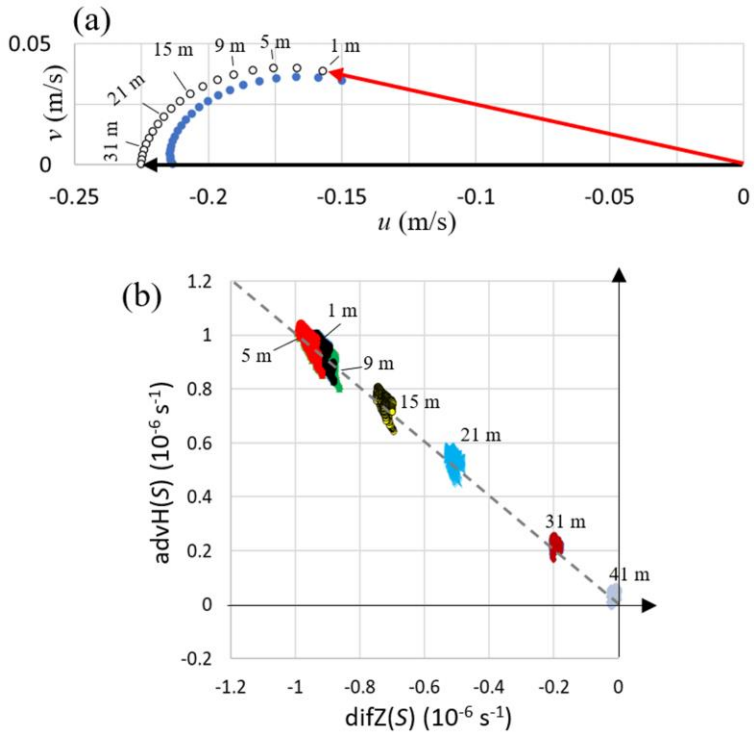

Figure 4: No-channel experiment. (a) Hodograph of bottom-parallel velocity components in the bottom Ekman layer, shown at a depth interval of 2 m. The open circles show the results for the control configuration, the filled circles for a neutral density field (N = 0). (b) Comparison of relative salinity changes induced by horizonal advection and vertical diffusion terms in equation (4) at different depth levels above the seafloor. Positive y values correspond to a relative salinity increase due to upslope advection. The broken line denotes the steady-state situation in which vertical diffusion effects fully offset horizontal advection effects.

3 Results and Discussion

3.1 No-channel Experiments

To establish the case, the first model runs using the control values (see Table) consider a continental slope devoid of submarine channels (H = 0). Discusses are the cases for (i) neutrally buoyant particles (w_s = 0) and (ii) negatively buoyant particles with a large settling speed of w_s = -5 mm s^{-1}. In the absence of other processes, this settling speed makes particles sink a distance of 50 m on a timescale of 2.5 hours. In this model application, this implies that all particles rapidly sink into the lowermost model layer, where random turbulent displacements keep them at a distance of a few meters from the seafloor.

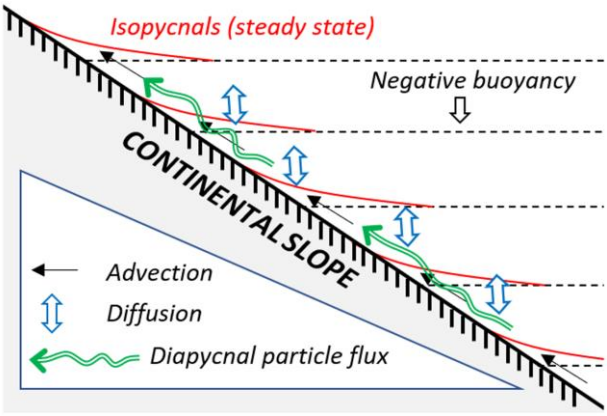

any

Figure 5: Schematic of an advective-diffusive balance facilitating an upslope sediment flux at continental margins.

The results demonstrate that the particles are systematically moved diapycnally across salinity surfaces and diagonally upward on the continental slope (**Figure 3a-b**). Interestingly, this upslope sediment flux becomes enhanced in the presence of vertical particle settling. Both features are explained by the vertical structure of the bottom Ekman layer (**Figure 4a**). The flow throughout this layer has an upslope component. The greatest upslope speed establishes within 10 m from the seafloor, whereas the flow is more aligned with isobaths at distances > 30 m. Under the effect of gravitational settling, an increasing number of particles becomes concentrated near the seafloor, where the swiftest upslope flow occurs. This increases the fraction of particles upwelling along the slope. In addition, analysis of terms in the salinity conservation equation (4) reveal that, at all vertical levels, the upslope salinity advection in this Ekman layer is almost perfectly offset by vertical salinity diffusion (**Figure 4b**). Due to this advective-diffusive balance, the salinity field becomes “arrested”. Nevertheless, particles are not constrained by this type of diffusion and they are moved unhindered upward on the continental slope, even more so if gravitational settling keeps them concentrated near the seafloor (see Fig. 3) where the swiftest upslope flow is situated. This mechanism, illustrated in **Figure 5**, is fundamental for upslope particle fluxes at continental margin. It should be emphasized that a

slope current with the opposite direction would create a bottom Ekman layer inducing downwelling rather than upwelling. Hence, the upwelling mechanism is direction dependent.

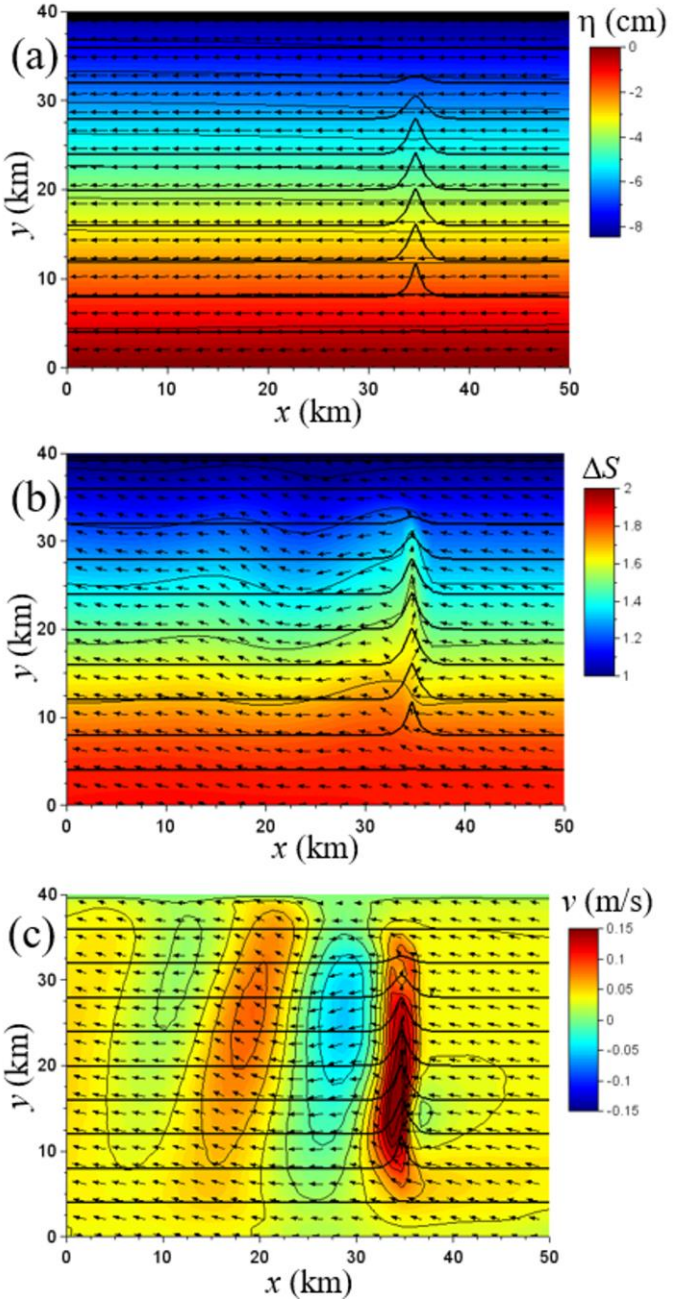

Figure 6: Experiment A. Horizontal distributions (think lines and shading) after 5 days of simulation of a) sea-surface elevation (cm), b) near-bottom salinity anomalies, and c) upslope velocity component v (m s^{-1}). Thick lines are bathymetric contours (CI = 100 m). Arrows are horizontal velocity vectors.

3.2 Channel Experiments

The forcing creates a slope current that approaches the submarine channel right-bounded by shallower water and opposite to the phase propagation direction of free topographic Rossby waves (**Figure 6**). The resultant surface geostrophic current is largely unidirectional and at a speed of ~0.2 m/s (**Figure 6a**). The sea-level gradient driving this flow is of the order of 1 cm per 5 km. Flow-bathymetry interactions create a stationary topographic Rossby wave confined to a near-bottom layer. In Experiment A, this wave has a horizontal wavelength of 12-15 km. As a result of this wave, the near-bottom salinity field develops a meandering pattern with salinity anomalies of ~0.1 (**Figure 6b**). Associated with this wave are alternating zones of upslope and downslope flows with speeds of up to 0.2 m/s (**Figure 6c**). More importantly, the axis of the submarine channel coincides with a zone of persistent up-channel flow (which is the origin of Rossby-wave generation) that continues to exist for the entire 10-day simulation.

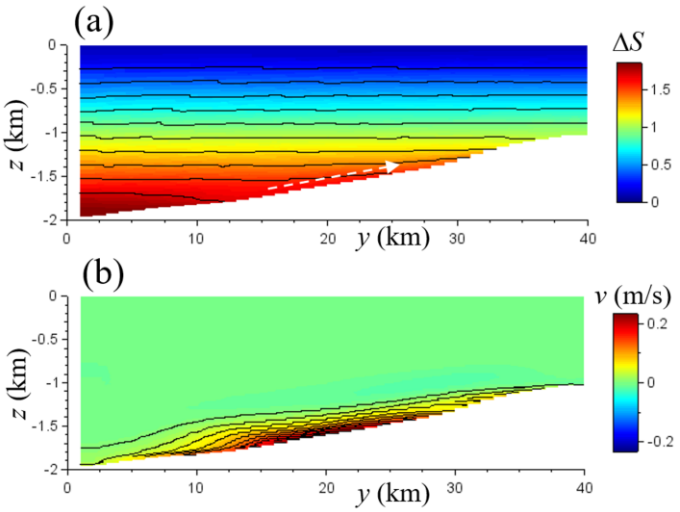

Figure 7: Experiment A. Vertical transect at x = 35 km (along the channel axis) after 5 days of simulation of a) salinity anomaly (relative to a constant value of 34; color shading and contours), and b) upslope velocity component (m/s; color shading and contours). In this display, the salinity and velocity fields in σ coordinates were mapped onto a Cartesian coordinate system with a vertical grid spacing of 1 m.

The wave disturbances developing here are confined to the near-bottom layer of the water column and have no surface expression (**Figure 7**). The up-channel flow is bottom-intensified and confined to the lowermost ~100 m of the water column, which coincides roughly with the channel depth. Despite the existence of the persistent up-channel flow, the salinity field establishes a steady-state distribution within a few days of simulation. Again, we can test this steady state with an analysis of relative effects of advection and diffusion in the salinity budget. Similar to the Ekman-layer experiment (see Fig. 4b), this analysis reveals a high degree of diffusive compensation of advective effects within the lowermost ~10 m of the water column (**Figure 8**). This compensation occurs along the up-channel flow in the submarine channel.

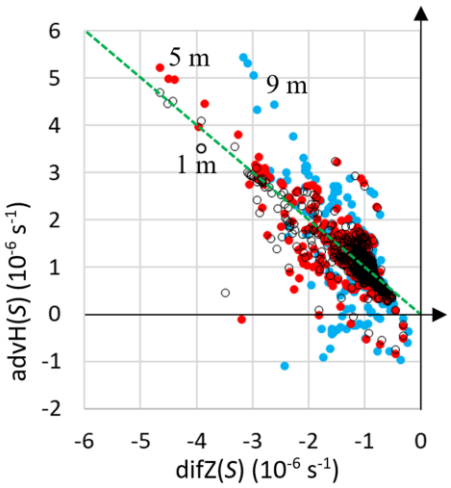

Figure 8: Same as Fig. 4b, but for Experiment A after 5 days of simulation.

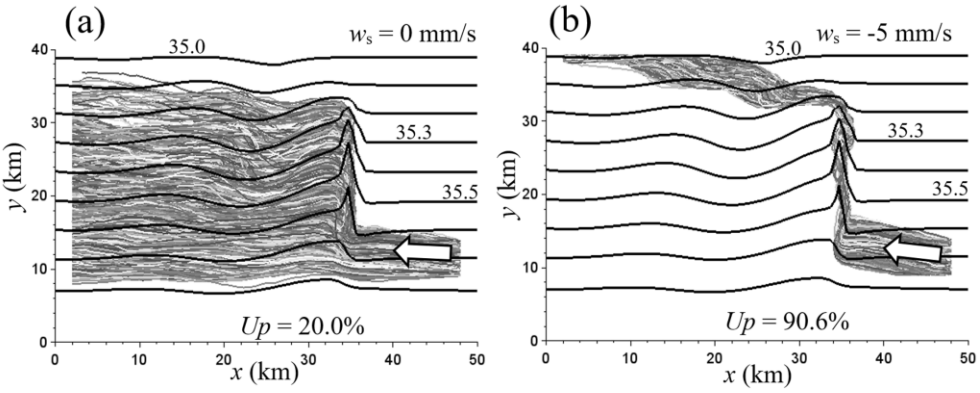

Figure 9: Same as Fig. 3, but for Experiment A.

It is this advective-diffusive balance that facilitates the upslope diapycnal transport of particles (**Figure 9**). For neutrally buoyant particles, the upslope displacement distance depends mainly on the vertical positioning of particles. Due to this vertical spread of particles, as the particle stream reaches the channel, particles become spread over most of the continental slope (**Figure 9a**). Particles that remain located close to the seafloor experience the largest upslope displacement.

This feature becomes accentuated for negatively buoyant particles that due to their high settling speed (w_s = -5 mm s^{-1}) become entrapped in the up-channel flow and form a concentrated particle stream (**Figure 9b**). This particle stream transverses the model's continental slope at speeds of up to 0.2 cm s^{-1} on a timescale of a few days. To the end, the head of the submarine channel serves as a bottleneck for upslope particle fluxes. In this experiment, almost all (90.6%) particles are upwelled to total water depths <1500 m.

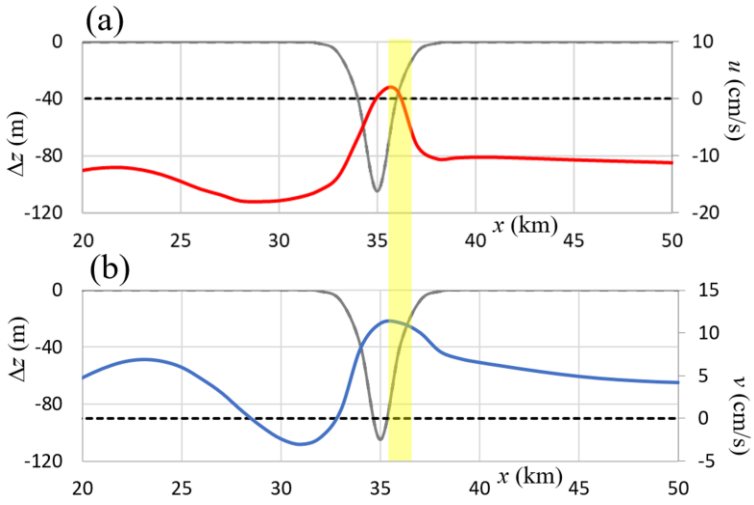

Figure 10: Experiment A. Velocity components *u* and *v* (cm/s) across the submarine channel at *y* = 20 km (where the ambient total water depth is 1500 m). The gray curve shows bathymetric variations. The yellow bar illustrates the zone of horizontal convergence around a vanishing *u* in conjunction with upslope flow ($v > 0$).

In the Ekman-layer experiment, particles ascended upward on the continental slope in a diagonal fashion (see Fig. 3). In stark contrast to this, in the presence of a submarine channel, flow-bathymetric interactions create a zone in which the particle transport inside the channel is perpendicular to the ambient isobaths. This feature is associated with the existence of a zero crossing of the *u* component (**Figure 10a**) in conjunction with a zone of both a horizontal flow convergence, $\partial u/\partial x < 0$, which keeps negatively buoyant particles trapped, and an upslope *v* component (**Figure 10b**) as the agent of the concentrated upslope particle stream.

For comparison, let us focus on Experiment B using a wider (W = 10 km) and deeper (H = 200 m) submarine channel with otherwise unchanged parameter settings. Again, the canyon-flow interaction leads to the formation of a stationary topographic Rossby wave that, again, is confined to the near-bottom layer of the water column (**Figure 11a-b**). The resultant wavelength of ~35 km is twice that observed in Experiment A (see Fig. 6b). The generation of this wave is related to a narrow zone of upslope flow with speeds of 15 cm s^{-1} located on the upstream side of the channel (**Figure 11b**). The width of this zone is only 2-4 km. On the other hand, a recirculation forms in the lower reaches of the submarine channel (**Figure 11c)**. Kämpf (2006) described similar eddy-type features in the lower portions of submarine canyons.

Again, neutrally buoyant particles become dispersed over most of the continental slope in interaction with the submarine channel (**Figure 12a**). Eddy formation in lower portions of the submarine channel induces the trapping of a relatively large fraction (10.9%) of particles after 10 days of simulation. This trapping feature relies on the existence of a channel mouth. With the inclusion of gravitational settling, which keeps particles close to the seafloor, the narrow zone of upslope flow on the channel's upstream side sets up a distinct route for the upslope transport of

particles (**Figure 12b**), similar to that observed in Experiment A (see Fig. 9b). Indeed, such routes can only exist, if the turbulence within the upslope flow keeps the particles in suspension. It should be noted that the wide U-shaped submarine channel of Experiment C creates a particle transport pattern that is very similar to that of Experiment B (**Figure 12c-d**, compare with Fig. 12.a-b). In experiments B and C, the narrow zone of upslope flows coincides again with zero crossing of the *u* component and a horizontal flow convergence (results not shown).

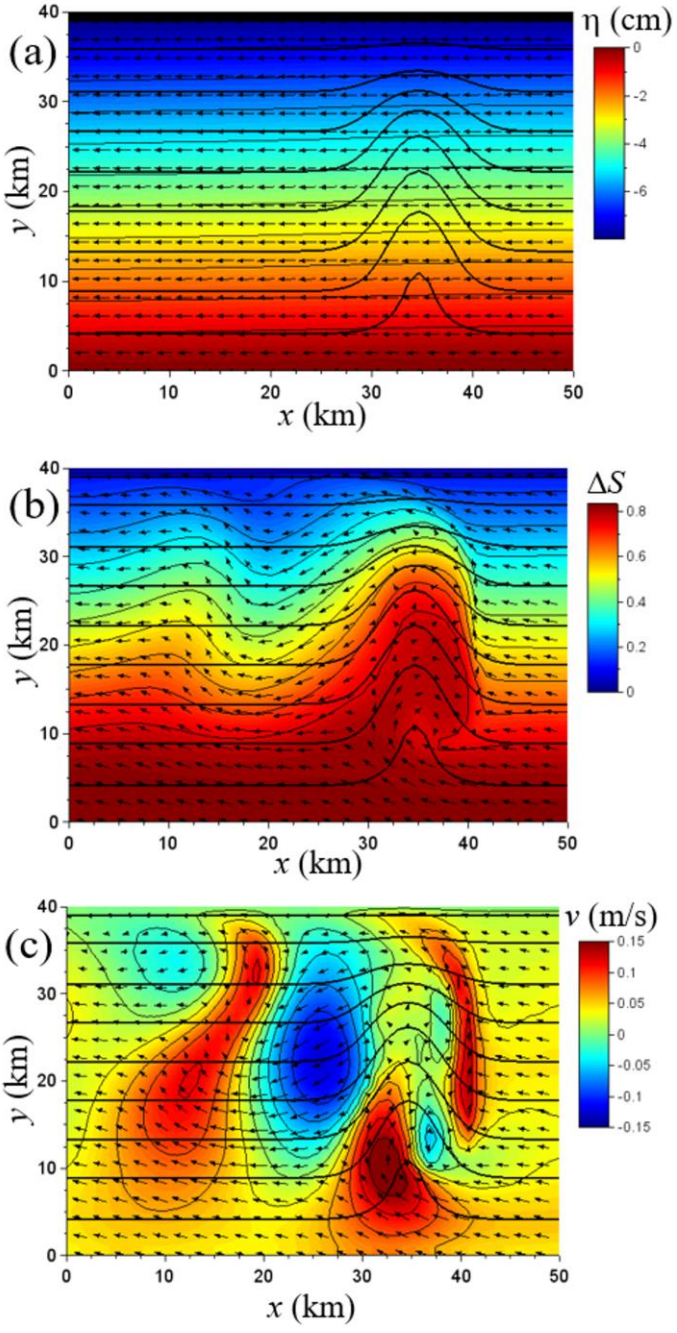

Figure 11: Same as Fig. 6, but for Experiment B (see Fig. 2a).

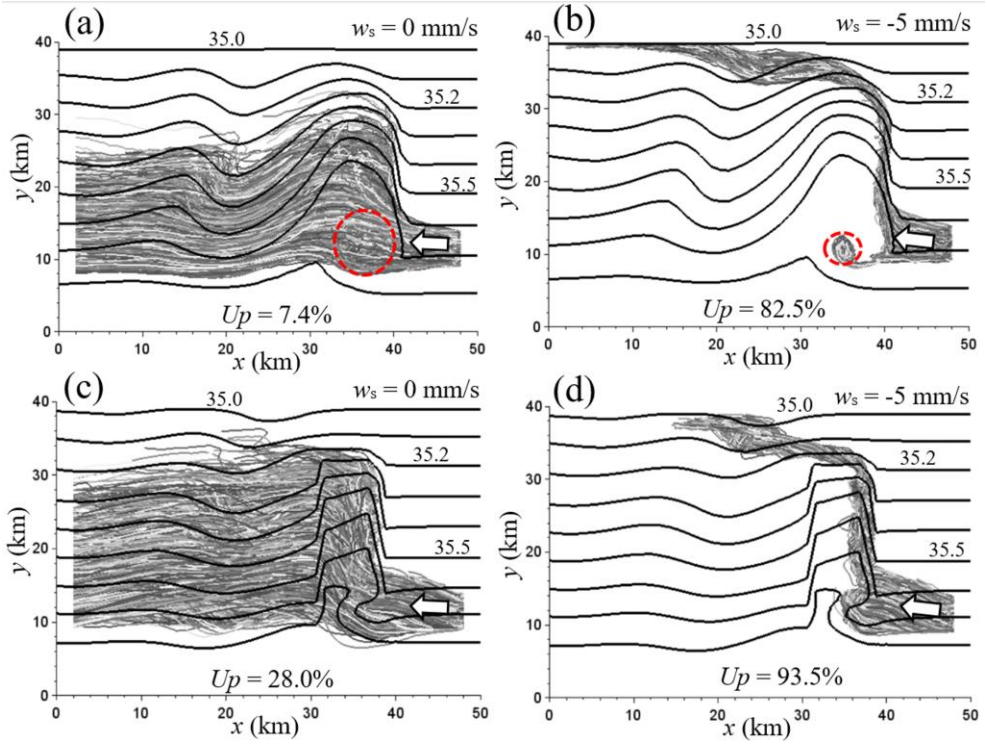

Figure 12: Same as Fig. 9, but panels a) and b) show the results for Experiment B, and panels c) and d) for Experiment C (see Fig. 2a). The red circles denote local trapping zones.

For a given channel depth, the general features of the results are invariant on the particular shape of the submarine channel. For instance, a U-shaped channel of 7 km width and 100 m depth yields results similar to those of the control experiment (**Figure 12c-d)** compare with Fig. 9). It should be noted that, similar to the results for a wide channel (see Fig. 11b), the zone of upslope flow is located on the upstream side of the channel.

Given the fundamental process of Rossby-wave formation, it may not be surprising to see that all experiments outlined in Table 1 create an upslope flow inside the submarine channel (**Figure 13**). Hence, the existence of such upslope flows is a fundamental feature, but what varies are the speed of upslope flows and the wavelength of Rossby waves. It is outside the scope of this study to derive the functional relationships between parameters. Nevertheless, it is worthwhile to summarize key findings (results not shown). a) Most experiments listed in Table 1 create distinct upslope transport routes for negatively buoyant particles. b) The speed of up-channel flows decreases significantly for smaller channel depths and/or reduced stability frequency. The existence of vertical density stratification is an essential condition for the proposed upwelling mechanism. c) Predicted up-channel speeds vary by only <10% for variations of vertical eddy diffusivity, D_z, over 2 orders of magnitude. While variations of D_z influence the degree of near-bottom perturbations of the steady-state density field, the upslope particle flux remains largely unaffected by this. This implies that, under the assumption that particles remain suspended in the water column, vertical mixing is not required to create the

advective particle flux. Instead, the cause-and-effect relationship is the other way around. The Rossby-wave disturbance initiates an advective particle flux inside the channel that becomes modified by the ambient turbulence levels, that also influence the ambient density field.

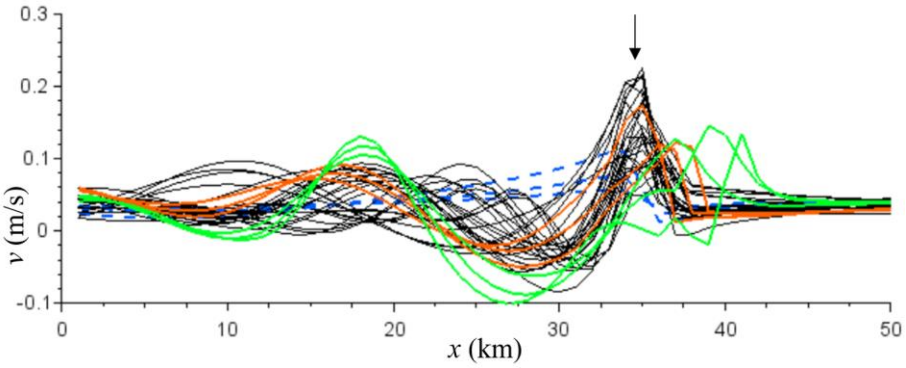

Figure 13: Structure of the upslope velocity component in the lowermost model layer along y = 20 km for all (40) experiments listed in Table 1. Dashed blue lines show the results for three different narrow channels (W = 5 km; see Fig. 2a) in the presence of weak density stratification ($N = 0.86\times10^{-3}$ s^{-1}). Green curves show results for the three U-shaped channels (see Fig. 2b), red curves for the three wider channels (see Fig. 2b), all for the control configuration ($N = 2.17\times10^{-3}$ s^{-1}. Note that axis of the zone of upslope flows is shifted upstream relative to the channel axis (highlighted by the arrow).

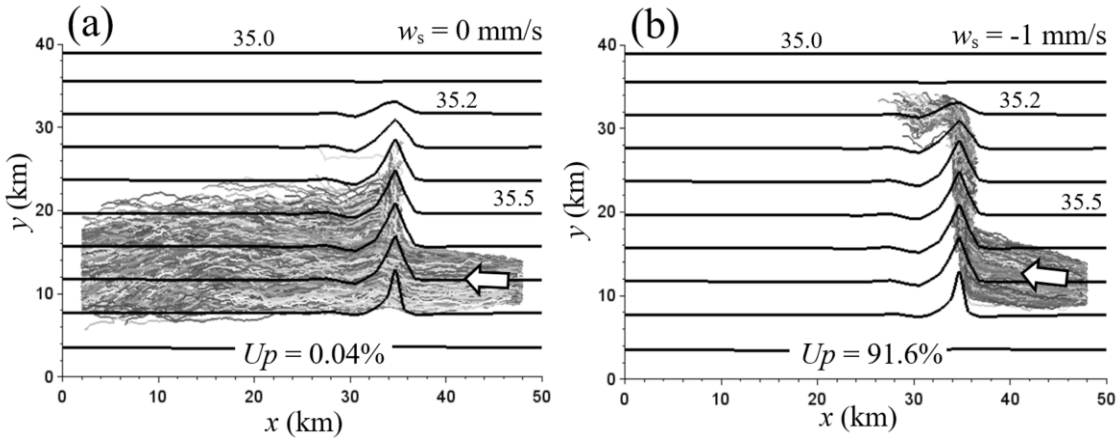

Figure 14: Same as Fig. 9, but for the slow-flow experiment (see text) and for a total simulation time of 12 days.

It is important to stress that the proposed upwelling mechanism still develops for weaker slope currents. Figure 14 displays the results for a slope current of 5 cm s^{-1} in speed, noting that, in conjunction with weaker flows, the vertical eddy diffusivity has been reduced to a value of D_z = 0.002 m^2 s^{-1}, corresponding to a reduced Ekman layer depth of $\delta_E = \sqrt{2A_z/|f|} \approx$ 6.3 m. This

setting creates an up-channel flow of 3 cm s^{-1} and a distinct upslope transport route for negatively buoyant particles (**Figure 14b**). Indeed, such sediment transport routes rely on the existence of sufficiently high levels am ambient turbulence keeping the particles in suspension.

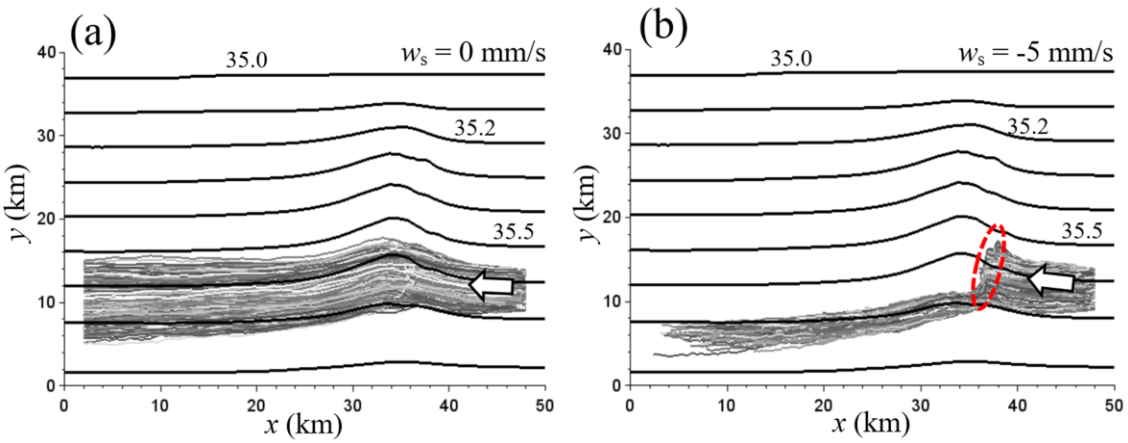

Figure 15: Same as Fig. 9, but for a sign reversal of the Coriolis parameter, which creates a slope current propagating into the same direction as the topographic Rossby waves it creates. The red ellipse in panel b) denotes a zone of particle trapping.

Finally, the author wishes to present a scenario that creates fundamentally different results, namely that of a slope current that travels into the same direction as topographic Rossby waves. Standing Rossby waves cannot form in this case, and neutrally buoyant particles are advected with little interaction across the submarine channel (**Figure 15a**). On the other hand, negatively buoyant particles become trapped in a zone of horizontal flow convergence, but without any signs of upwelling (**Figure 15b**).

4 Conclusion

This work reveals a physical process that operates to return particulate matter upslope on continental margins inside deep-sea submarine channels. This upslope sediment transport is made possible from the interaction of a slope current that, due to water-column stretching, creates a narrow zone of upslope flow along the submarine channel. This disturbance is the starting point for the creation of a stationary topographic Rossby wave. Due to diffusive countereffects, the ambient stratified water column is not significantly affected by this wave. Hence, the density field does not infer the existence of swift diapycnal currents. The associated bottom-intensified velocity field creates a distinct pathway for the upslope transport of suspended particles that upwell over depth ranges of kilometres on short timescales of days. If energetic enough, the up-channel flows may create their own turbulence hindering sediment settling. Otherwise, tidal currents and/or internal waves, not considered in this study, may assist in keeping particles in suspension, as observed in the upper Whittard Canyon (Amaro *et al.*, 2015; 2016).

Field observations inside the Whittard Canyon (NE Atlantic) provide evidence of continuous up-canyon currents, which agrees with the findings presented here, but there are no direct records of ambient slope currents, which makes the agreement incomplete. More field studies including mooring observations adjacent to submarine channels/canyons are required to verify the proposed mechanism. Future theoretical studies should consider more realistic representations of bathymetry, turbulence, suspended sediment dynamics and seabed interactions, which were highly simplified in this work.

Acknowledgments

The author is grateful to the late Matthias Tomczak for discussions on early versions of this research. The author thanks two anonymous reviewers for their constructive criticisms that helps to significantly improve the quality of the work. The author has no real or perceived financial conflicts of interests of any kind. This work uses the original version of the COHERENS model (Luyten *et al.*,1999). The FORTRAN code of the model with the configuration for Experiment A including data outputs and instructions are available from doi:10.5281/zenodo.4065221. This research has not received external research funding.

References

Alberty, M. S., Billheimer, S., Hamann, M. M., Ou, C. Y., Tamsitt, V., Lucas, A. J., & Alford, M. H. (2017), A reflecting, steepening, and breaking internal tide in a submarine canyon. *Journal of Geophysical Research-Oceans*, 122, 6872–6882, doi:10.1002/2016JC012583.

Allen, S. E., Vindeirinho, C., Thomson, R. E., Foreman, M. G., & Mackas, D. L. (2001), Physical and biological processes over a submarine canyon during an upwelling event. *Canadian Journal of Fisheries and Aquatic Sciences*, 58(4), 671– 684. doi:10.1139/f01-008.

Allen, S., & Durrieu de Madron, X. (2009), A review of the role of submarine canyons in deep-ocean exchange with the shelf. *Ocean Science*, 5, 607–620.

Amaro, T., de Stigter, H., Lavaleye, M., & Duineveld, G. (2015), Organic matter enrichment in the Whittard Channel (northern Bay of Biscay margin, NE Atlantic); its origin and possible effects on benthic megafauna. *Deep-Sea Research Part I*, 102, 90–100.

Amaro, T., Huvenne, V. A. I., Allcock, A. L., Aslam, T., Davies, J. S., Danovero, R., De Stigter, H. C., Duineveld, G. C. A., Gambi, C., Gooday, A. J., Gunton, L. M., Hall, R., Howell, K. L., Ingels, J., Kiriakoulakis, K., Kershaw, C. E., Lavaleye, L. S. S., Robert, K., Stewart, H., Van Rooij, D., White, M., & Wilson, A. M. (2016), The Whittard Canyon: a case study of submarine canyon processes. *Progress in Oceanography*, 146, 38–57. doi:10.1016/j.pocean.2016.06.003.

Blumberg, A. F., & Mellor, G. L. (2013), A description of a three-dimensional coastal ocean circulation model. In Three-Dimensional Coastal Ocean Models, N.S. Heaps (Ed.). doi:10.1029/CO004p0001.

Bosley, K. L., Lavelle, J. W., Brodeur, R. D., Wakefield, W. W., Emmett, R. L., Baker, E. T., & Rehmke, K. M. (2004), Biological and physical processes in and around Astoria submarine Canyon, Oregon, USA. *Journal of Marine Systems*, 50(1), 21-37.

Cacchione, D. A., Pratson, L.F., & Ogston, A. S. (2002), The shaping of continental slopes by internal tides. *Science*, 296, 724, doi:10.1126/science.1069803.

Freeland, H., & Denman, K., (1982), A topographically controlled upwelling center off Vancouver Island. *Journal of Marine Research*, 40, 1069–1093.

Hentschel, B., & Shimeta, J. (2008), Suspension feeders. In: Jorgensen, S. (ed), *Encyclopedia of Ecology*. Elsevier, Amsterdam, pp 3437–3442.

Hickey, B. M. (1997), The response of a steep-sided, narrow canyon to time-variable wind forcing. *Journal of Physical Oceanography*, 27(5), 697–726, doi:10.1175/1520-0485(1997)027<0697:TROASS>2.0.CO;2.

Hotchkiss, F., & Wunsch, C. (1982), Internal waves in Hudson Canyon with possible geological implications. *Deep-Sea Research*, 29 (1982), 415-442.

Kämpf, J. (2006), Transient wind-driven upwelling in a submarine canyon: a process-oriented modelling study. *Journal of Geophysical Research*, 111, C11011, doi:10.1029/2006JC003497

Kämpf, J. (2012), Lee effects of localized upwelling in a shelf-break canyon. *Continental Shelf Research*, 42, 78–88. doi:10.1016/j.csr.2012.05.005.

Kämpf., J., (2018), On the dynamics of canyon–flow interactions. *Journal of Marine Science and Engineering*, 6(4), 129. doi:10.3390/jmse6040129.

Klinck, J. (1996), Circulation near submarine canyons: A modeling study. *Journal of Geophysical Research*, 101, 1211–1223. doi:10.1029/95jc02901.

Kunze, E., Rosenfeld, L. K., Carter, G. S., & Gregg, M. C. (2002), Internal waves in Monterey Submarine Canyon. *Journal of Physical Oceanography*, 32, 1890–1913.

Kunze, E., MacKay, C. McPhee-Shaw, E. E., Morrice, K. Girton, J. B., & Terker, S. R. (2012), Turbulent mixing and exchange with interior waters on sloping boundaries. *Journal of Physical Oceanography*, 42, 910–927. doi:10.1175/JPO-D-11-075.1.

Luyten, P. J., Jones, J. E., Proctor, R., Tabor, A., Tett, P., & Wild-Allen, K. (1999), COHERENS - A Coupled Hydrodynamical-Ecological Model for Regional and Shelf Seas: User Documentation; MUMM Report; Management Unit of the North Sea: Brussels, Belgium, 914p.

Maier-Reimer, E., (1980), On the formation of salt water wedges in estuaries. *Lecture Notes on Coastal and Estuarine Studies*, 1, 91–101.

McDonnell, A. M. P., & Buesseler, K. O. (2010), Variability in the average sinking velocity of marine particles. *Limnology and Oceanography*, 55, 2085–96. doi:10.4319/lo.2010.55.5.2085.

Middleton, J. F., & Bye, J. A. T. (2007), A review of the shelf-slope circulation along Australia's southern shelves: Cape Leeuwin to Portland. *Progress in Oceanography*, 75(1): 1–41, doi: 10.1016/j.pocean.2007.07.001.

Nazarian, R., & Legg, S. (2017a), Internal wave scattering in continental slope canyons, part 1: Theory and development of a ray tracing algorithm. *Ocean Modelling*, 118, 1–15. doi:10.1016/j.ocemod.2017.07.002.

Nazarian, R., & Legg, S. (2017b), Internal wave scattering in continental slope canyons, part 2: A comparison of ray tracing and numerical simulations. *Ocean Modelling*, 118, 16–30. doi:10.1016/j.ocemod.2017.07.005.

Shchepetkin, A. F., & McWilliams, J. C. (2005), The regional oceanic modeling system (ROMS): a split-explicit, free-surface, topography-following-coordinate oceanic model. *Ocean Modelling*, 9(4), 347–404, doi:10.1016/j.ocemod.2004.08.002.

Puig, P., Greenan, B. J. W., Li, M. Z., Prescott, R. H., & Piper, D. J.W. (2013), Sediment transport processes at the head of Halibut Canyon, eastern Canada margin: An interplay between internal tides and dense shelf-water cascading. *Marine Geology*, 341, 14–28, doi:10.1016/j.margeo.2013.05.004.

Puig, P., Palanques, A., & Martín, J. (2014), Contemporary sediment-transport processes in submarine canyons. *Annual Review of Marine Science*, 6:1, 53–77, doi:10.1146/annurev-marine-010213-135037.

Vlasenko, V., Stashchuk, N. Inall, M. E., Porter, M., & Aleynik. D. (2016), Focusing of baroclinic tidal energy in a canyon. *Journal of Geophysical Research-Oceans*, 121, 2824–2840, doi:10.1002/2015JC011314.

Wåhlin, A. K. (2002), Topographic steering of dense water with application to submarine canyons. *Deep-Sea Research I*, 49, 305–320.

Waterhouse, A. F., Mackinnon, J. A. Musgrave, R. C. Kelly, S. M. Pickering, A., & Nash, J. (2017), Internal tide convergence and mixing in a submarine canyon. *Journal of Physical Oceanography*, 47, 303–322. Doi:10.1175/JPO-D-16-0073.1.

Yu, Q., Wang, Y., Gao, J., Gao, S., & Flemming, B. (2014), Turbidity maximum formation in a well-mixed macrotidal estuary: The role of tidal pumping, *Journal of Geophysical Research-Oceans*, 119, 7705–7724, doi:10.1002/ 2014JC010228.

Figure captions

Figure 1: Model bathymetry for experiment A (see Fig. 2a). Arrows indicate the direction of the ambient geostrophic flow. The red line indicates the deployment region of Lagrangian floats.

Figure 2: Different shapes of submarine channels considered in a sequence of model runs. Here Δx denotes the distance from the channel axis, and Δz the bathymetry relative to the ambient seafloor. Experiments A, B and C denote configurations of experiments that are discussed in detail in the text.

Figure 3: No-channel experiment. Trajectories of 2000 particles with a settling speed of a) w_s = 0 mm s^{-1} and b) w_s = -5 mm s^{-1}. The lines are steady-state isohalines of the salinity field in the bottom-nearest model layer. "Up" refers to the percentage of particles that reach a water depth >1500 m after 10 days of simulation.

Figure 4: No-channel experiment. (a) Hodograph of bottom-parallel velocity components in the bottom Ekman layer, shown at a depth interval of 2 m. The open circles show the results for the control configuration, the filled circles for a neutral density field (N = 0). (b) Comparison of relative salinity changes induced by horizonal advection and vertical diffusion terms in equation (4) at different depth levels above the seafloor. Positive y values correspond to a relative salinity increase due to upslope advection. The broken line denotes the steady-state situation in which vertical diffusion effects fully offset horizontal advection effects.

Figure 5: Schematic of an advective-diffusive balance facilitating an upslope sediment flux at continental margins.

Figure 6: Experiment A. Horizontal distributions (think lines and shading) after 5 days of simulation of a) sea-surface elevation (cm), b) near-bottom salinity anomalies, and c) upslope velocity component v (m s^{-1}). Thick lines are bathymetric contours (CI = 100 m). Arrows are horizontal velocity vectors.

Figure 7: Experiment A. Vertical transect at x = 35 km (along the channel axis) after 5 days of simulation of a) salinity anomaly (relative to a constant value of 34; color shading and contours), and b) upslope velocity component (m/s; color shading and contours). In this display, the salinity and velocity fields in σ coordinates were mapped onto a Cartesian coordinate system with a vertical grid spacing of 1 m.

Figure 8: Same as Fig. 4b, but for Experiment A after 5 days of simulation.

Figure 9: Same as Fig. 3, but for Experiment A.

Figure 10: Experiment A. Velocity components u and v (cm/s) across the submarine channel at y = 20 km (where the ambient total water depth is 1500 m). The gray curve shows bathymetric variations. The yellow bar illustrates the zone of horizontal convergence around a vanishing u in conjunction with upslope flow (v > 0).

Figure 11: Same as Fig. 6, but for Experiment B (see Fig. 2a).

612 **Figure 12:** Same as Fig. 9, but panels a) and b) show the results for Experiment B, and panels c)
613 and d) for Experiment C (see Fig. 2a). The red circles denote local trapping zones.

614 **Figure 13:** Structure of the upslope velocity component in the lowermost model layer along y =
615 20 km for all (40) experiments listed in Table 1. Dashed blue lines show the results for three
616 different narrow channels (W = 5 km; see Fig. 2a) in the presence of weak density stratification
617 ($N = 0.86\times10^{-3}$ s^{-1}). Green curves show results for the three U-shaped channels (see Fig. 2b), red
618 curves for the three wider channels (see Fig. 2b), all for the control configuration ($N = 2.17\times10^{-3}$
619 s^{-1}. Note that axis of the zone of upslope flows is shifted upstream relative to the channel axis
620 (highlighted by the arrow).

621 **Figure 14:** Same as Fig. 9, but for the slow-flow experiment (see text) and for a total simulation
622 time of 12 days.

623 **Figure 15:** Same as Fig. 9, but for a sign reversal of the Coriolis parameter, which creates a
624 slope current propagating into the same direction as the topographic Rossby waves it creates.
625 The red ellipse in panel b) denotes a zone of particle trapping.

626

627

628

629

630

631

632

633

634

635

Figure 1.

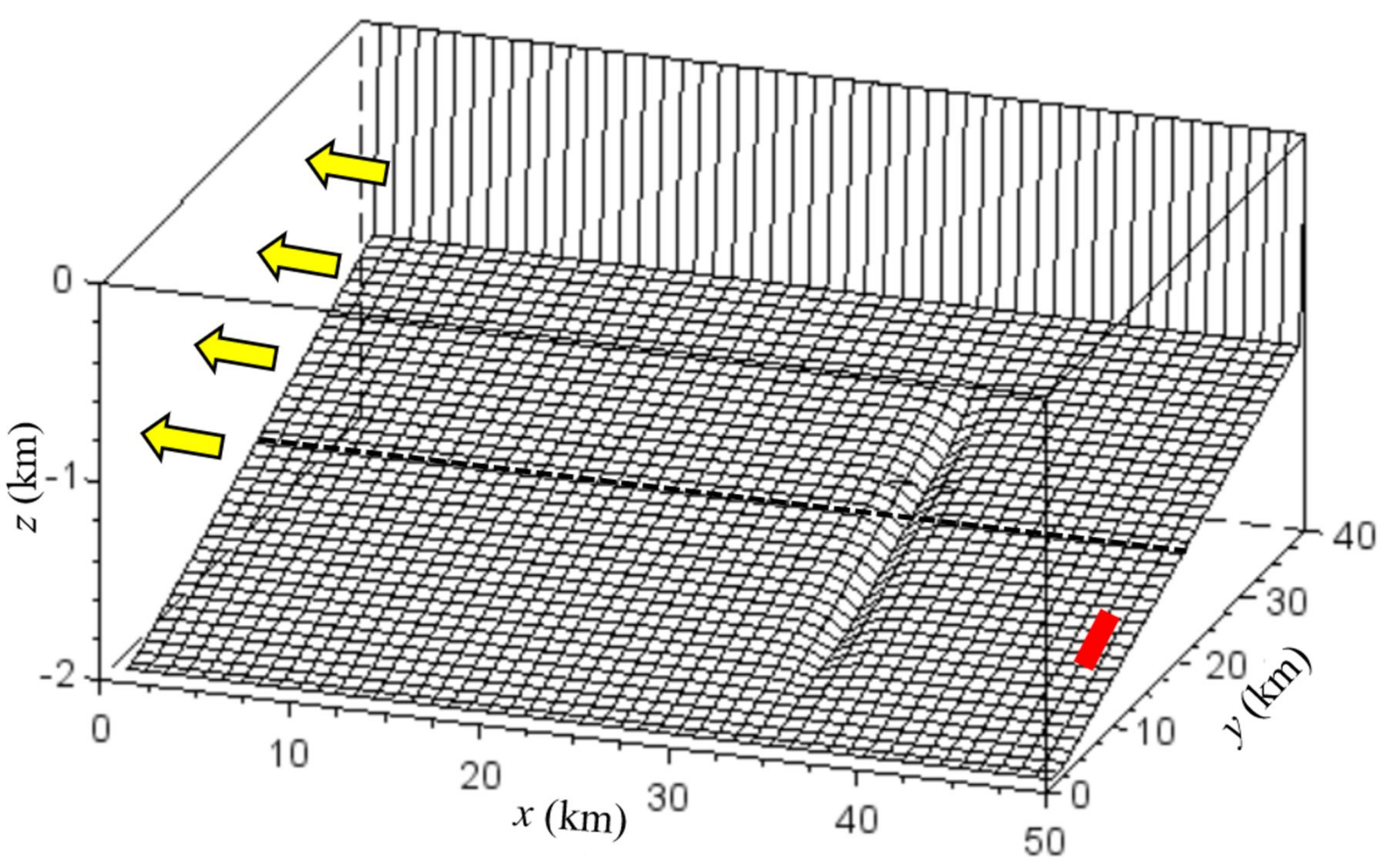
0
-1
-2
z (km)
0
10
20
30
40
50
x (km)
0
10
20
30
40
y (km)

Figure 2.

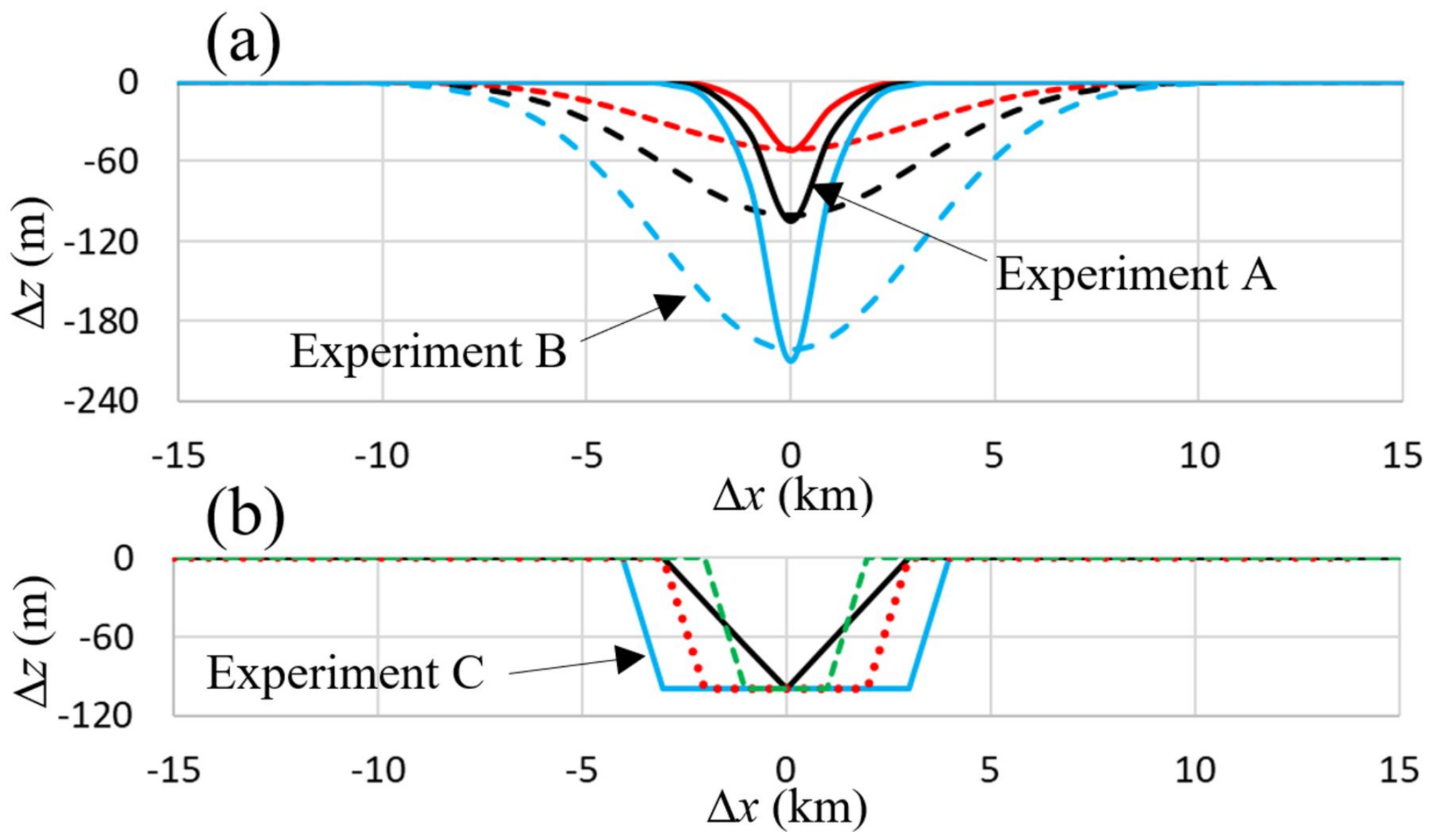
(a)
0
-60
-120
-180
-240
Δz (m)
Experiment A
Experiment B
-15
-10
-5
0
5
10
15
Δx (km)
(b)
0
-60
-120
Δz (m)
Experiment C
-15
-10
-5
0
5
10
15
Δx (km)

Figure 3.

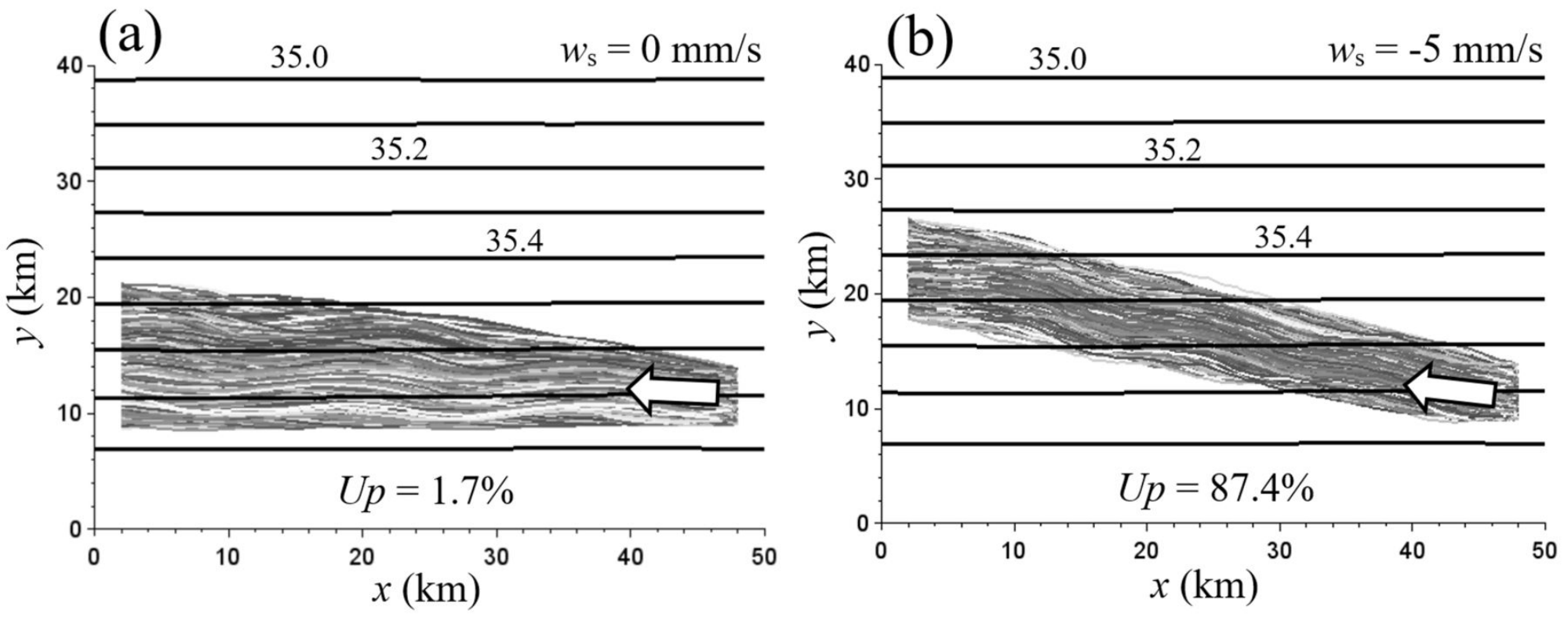
(a)
35.0
35.2
35.4
w_s = 0 mm/s
Up = 1.7%
y (km)
x (km)
(b)
35.0
35.2
35.4
w_s = -5 mm/s
Up = 87.4%
y (km)
x (km)

Figure 4.

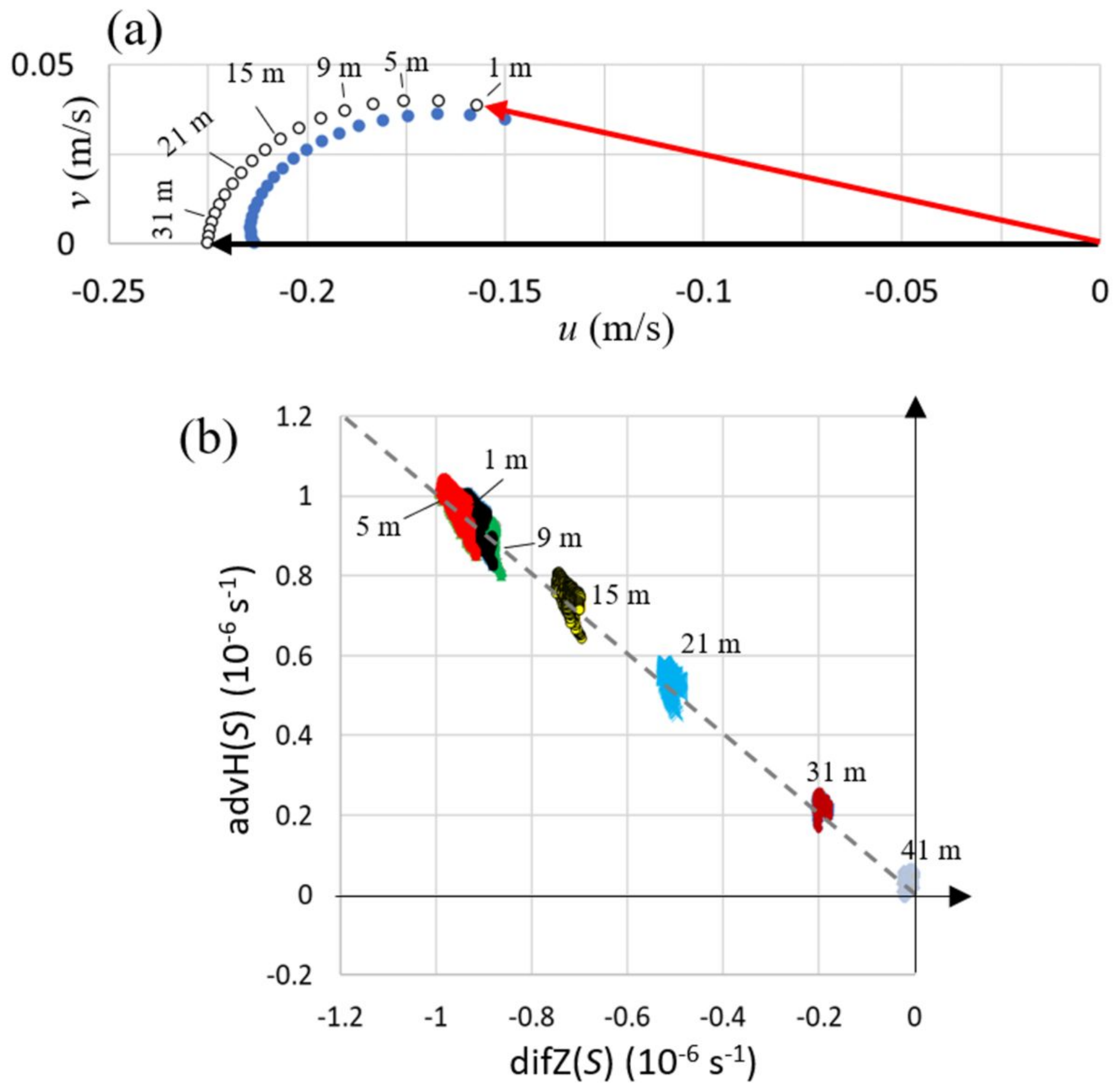
(a)
0.05
0
v (m/s)
1 m
5 m
9 m
15 m
21 m
31 m
-0.25
-0.2
-0.15
-0.1
-0.05
0
u (m/s)
(b)
1.2
1
0.8
0.6
0.4
0.2
0
-0.2
advH(S) (10-6 s-1)
1 m
5 m
9 m
15 m
21 m
31 m
41 m
-1.2
-1
-0.8
-0.6
-0.4
-0.2
0
difZ(S) (10-6 s-1)

Figure 5.

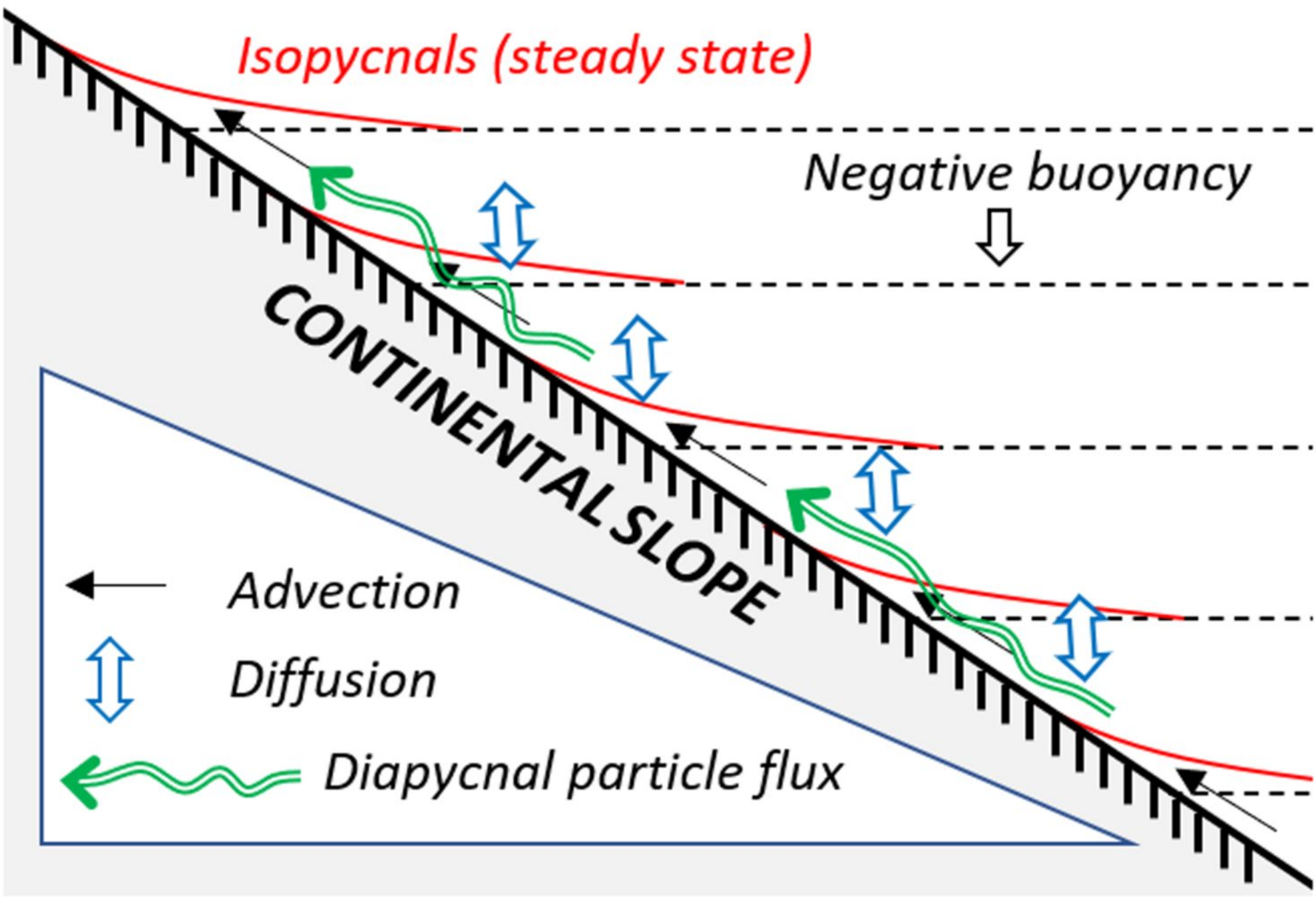
Isopycnals (steady state)
Negative buoyancy
CONTINENTAL SLOPE
Advection
Diffusion
Diapycnal particle flux

Figure 6.

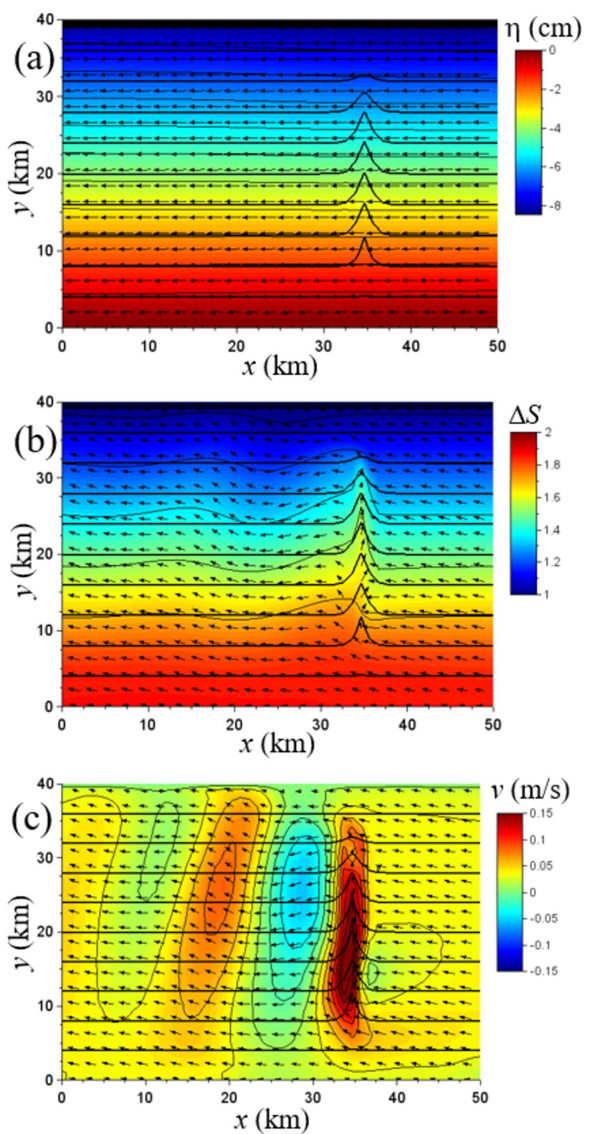
(a)
η (cm)
0
-2
-4
-6
-8
y (km)
x (km)
(b)
ΔS
2
1.8
1.6
1.4
1.2
1
y (km)
x (km)
(c)
v (m/s)
0.15
0.1
0.05
0
-0.05
-0.1
-0.15
y (km)
x (km)

Figure 7.

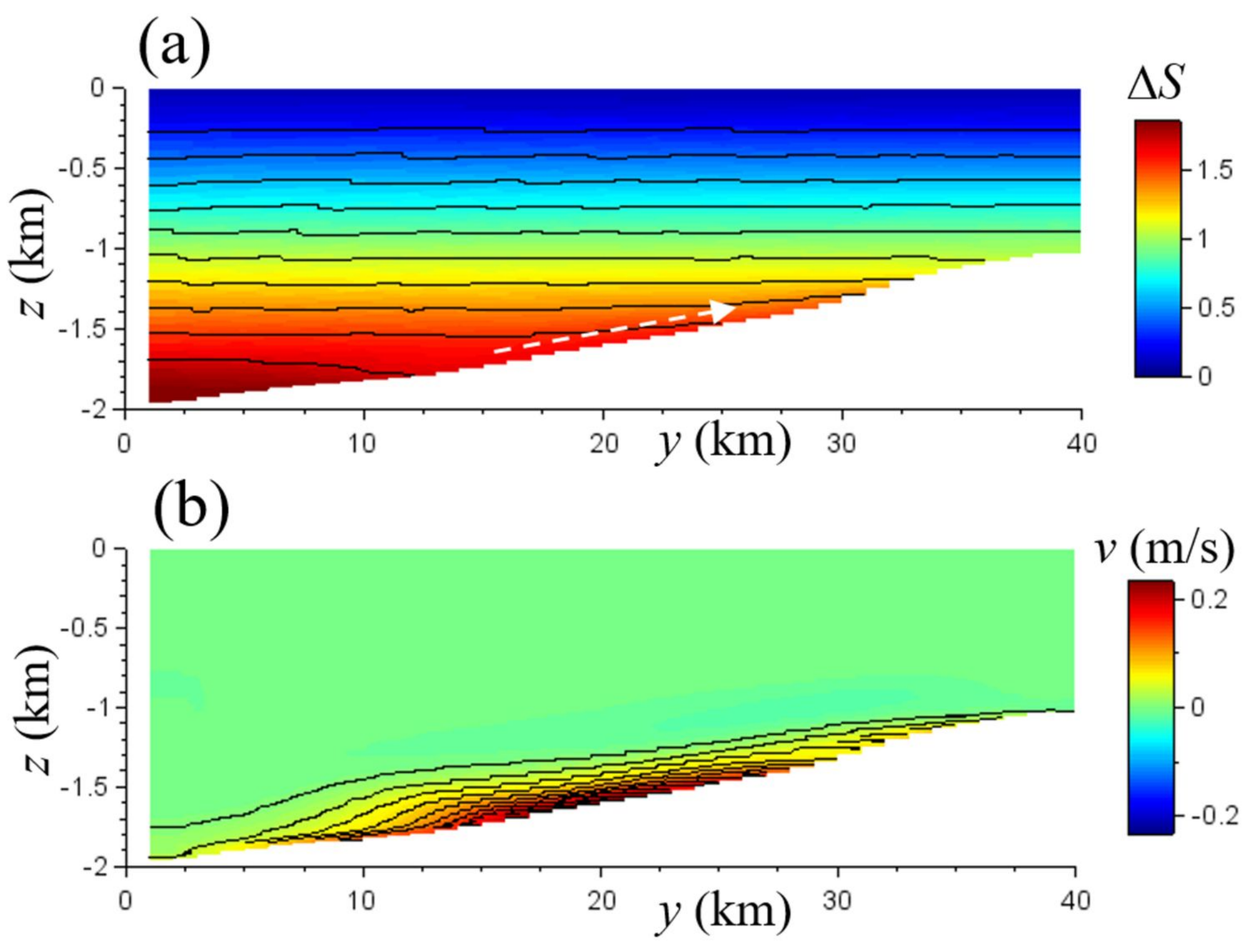
(a)
ΔS
1.5
1
0.5
0
z (km)
0
-0.5
-1
-1.5
-2
0
10
20
y (km)
30
40
(b)
v (m/s)
0.2
0
-0.2
z (km)
0
-0.5
-1
-1.5
-2
0
10
20
y (km)
30
40

Figure 8.

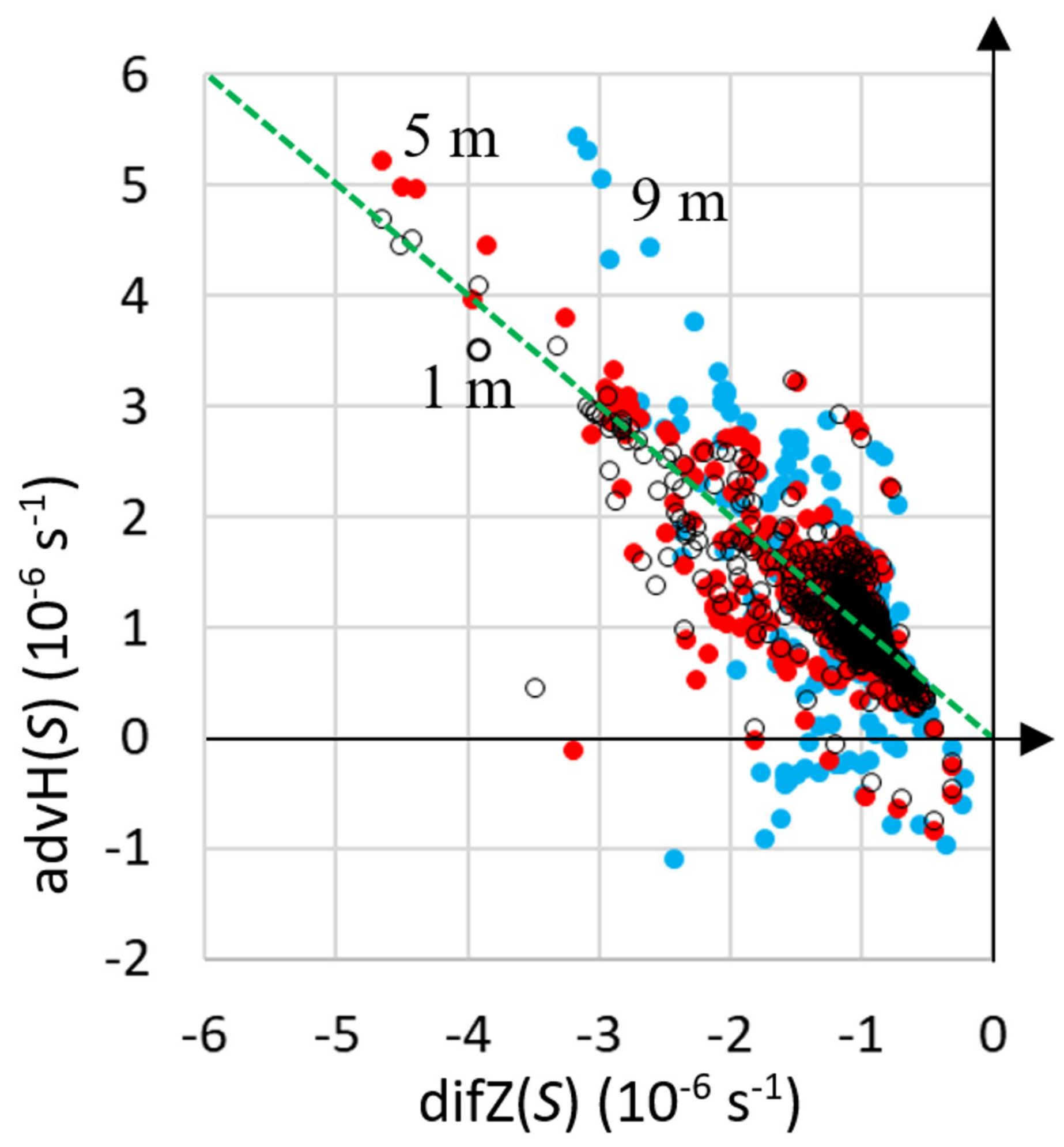
5 m
9 m
1 m
6
5
4
3
2
1
0
-1
-2
-6
-5
-4
-3
-2
-1
0
advH(S) (10-6 s-1)
difZ(S) (10-6 s-1)

Figure 9.

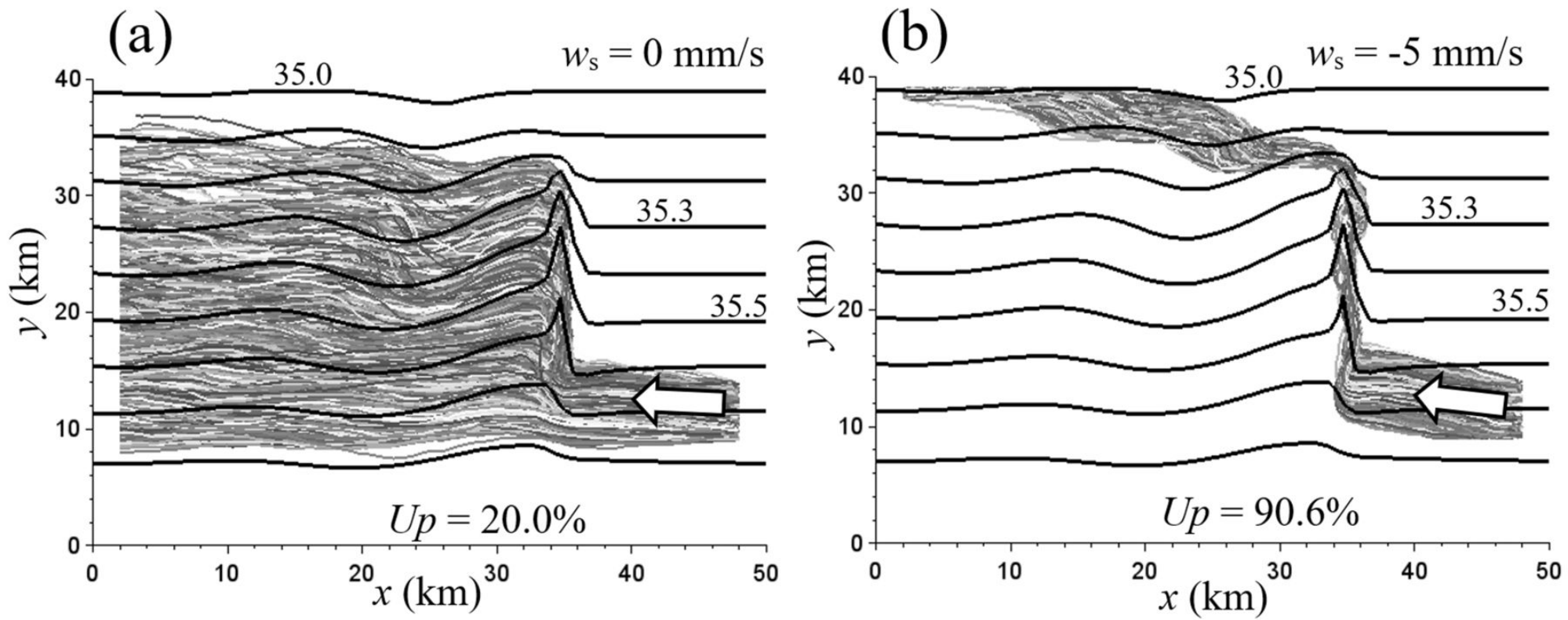
(a)
w_s = 0 mm/s
35.0
35.3
35.5
Up = 20.0%
y (km)
x (km)
(b)
w_s = -5 mm/s
35.0
35.3
35.5
Up = 90.6%
y (km)
x (km)

Figure 10.

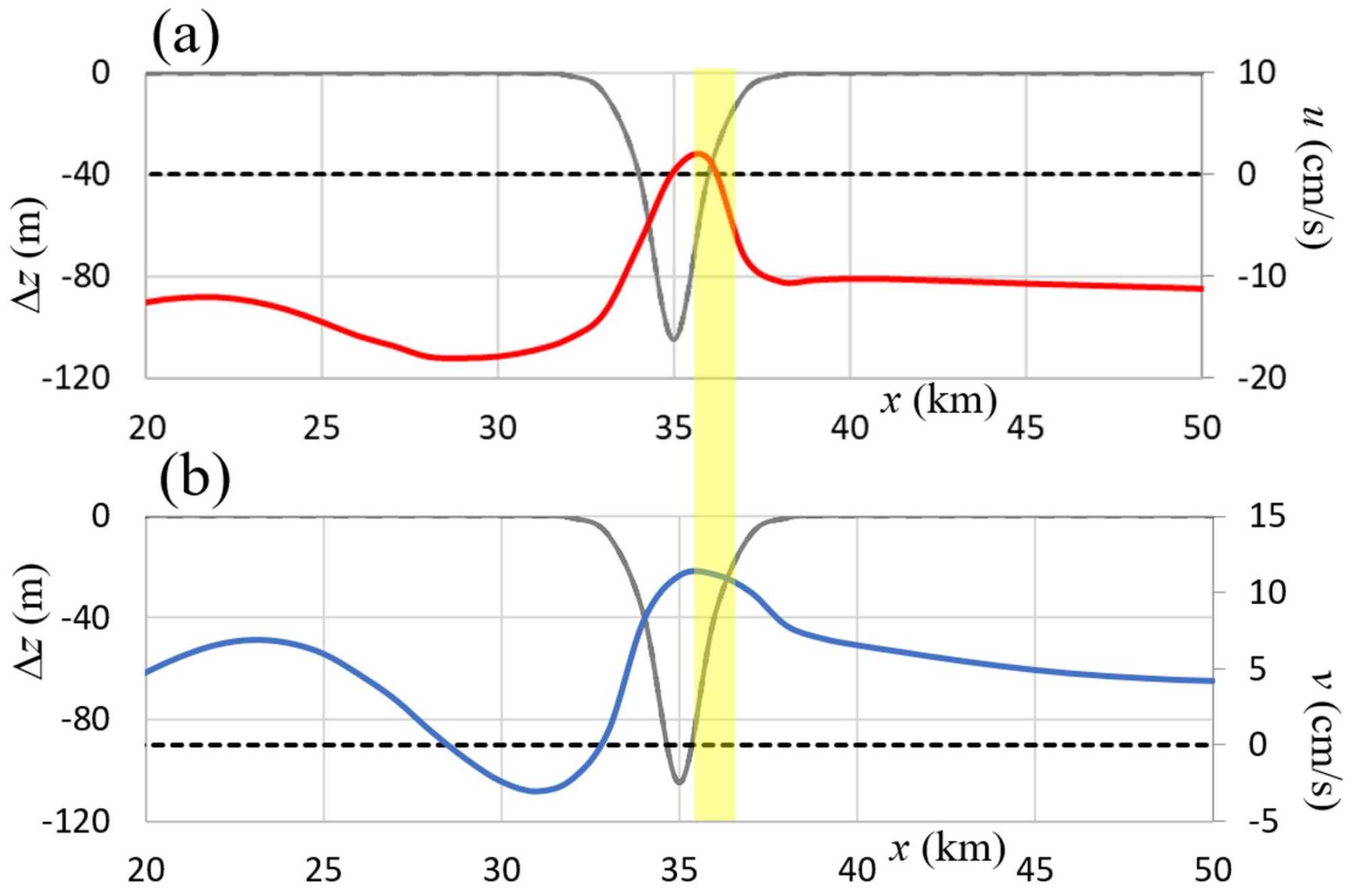
(a)
0
-40
-80
-120
Δz (m)
10
0
-10
-20
u (cm/s)
20
25
30
35
40
45
50
x (km)
(b)
0
-40
-80
-120
Δz (m)
15
10
5
0
-5
v (cm/s)
20
25
30
35
40
45
50
x (km)

Figure 11.

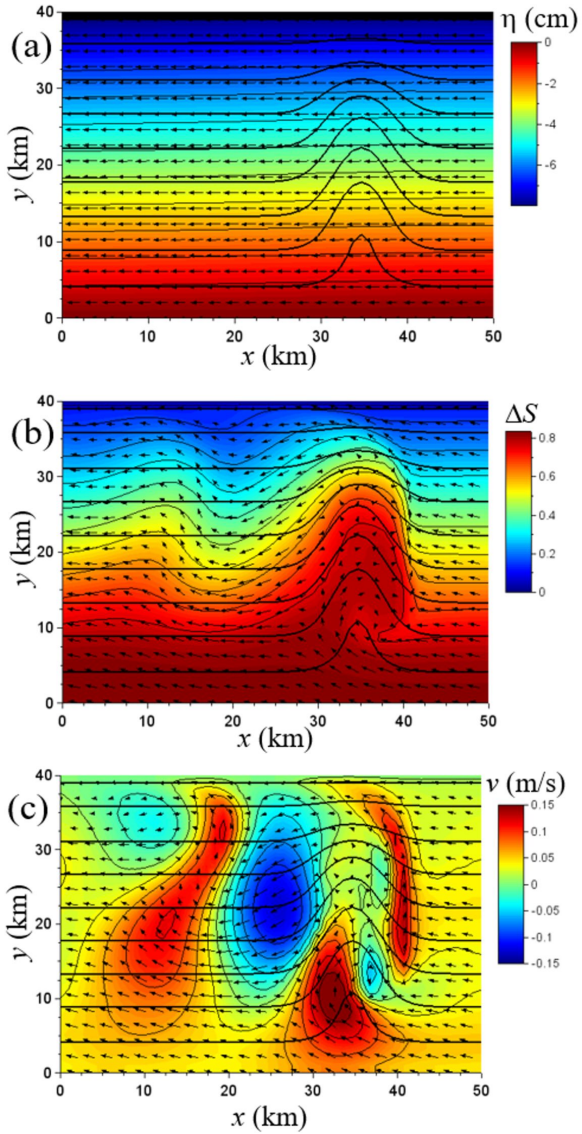
(a)
η (cm)
0
-2
-4
-6
y (km)
x (km)
(b)
ΔS
0.8
0.6
0.4
0.2
0
y (km)
x (km)
(c)
v (m/s)
0.15
0.1
0.05
0
-0.05
-0.1
-0.15
y (km)
x (km)

Figure 12.

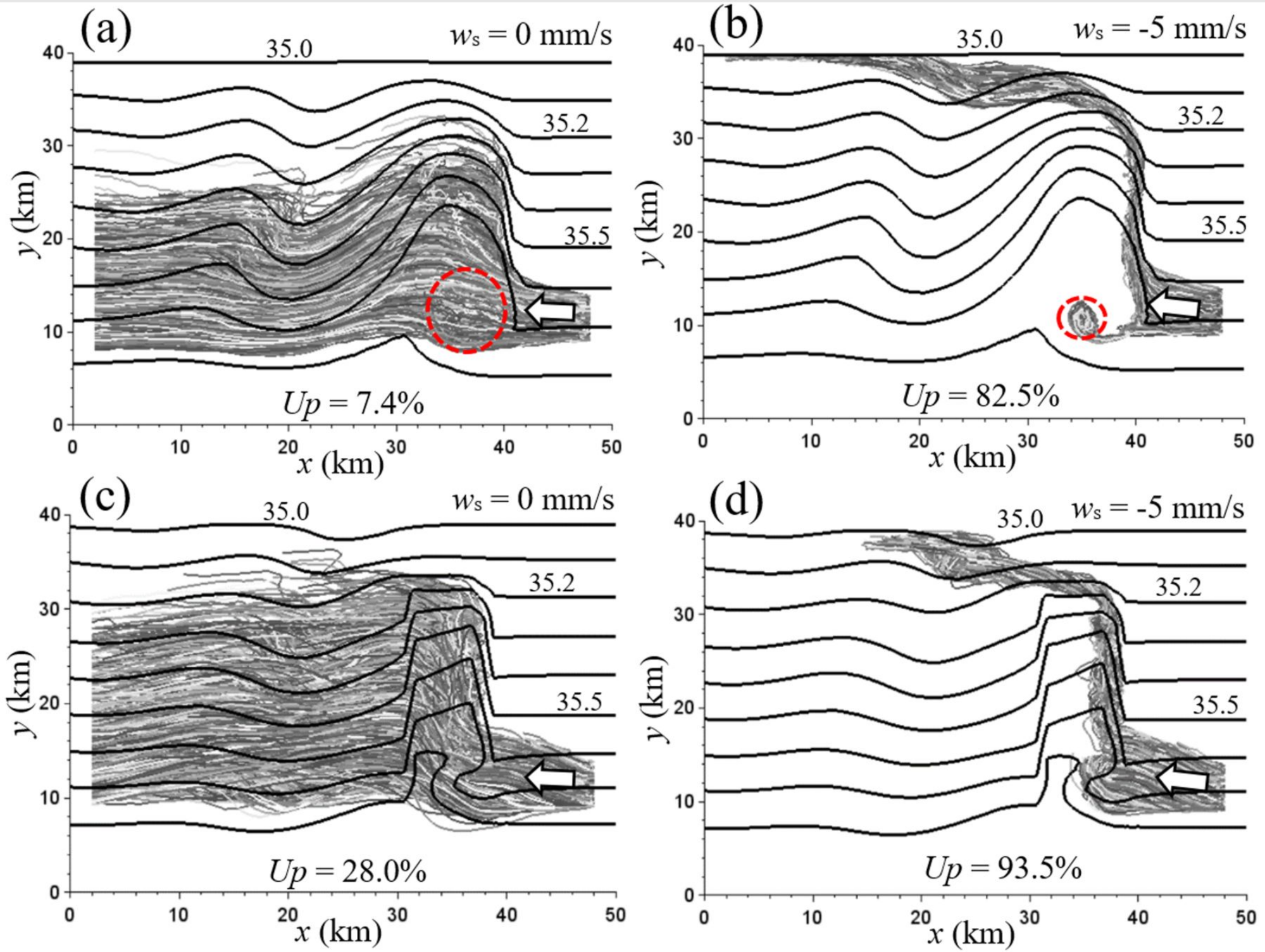
(a)
w_s = 0 mm/s
35.0
35.2
35.5
Up = 7.4%
(b)
w_s = -5 mm/s
35.0
35.2
35.5
Up = 82.5%
(c)
w_s = 0 mm/s
35.0
35.2
35.5
Up = 28.0%
(d)
w_s = -5 mm/s
35.0
35.2
35.5
Up = 93.5%
y (km)
x (km)
0
10
20
30
40
50

Figure 13.

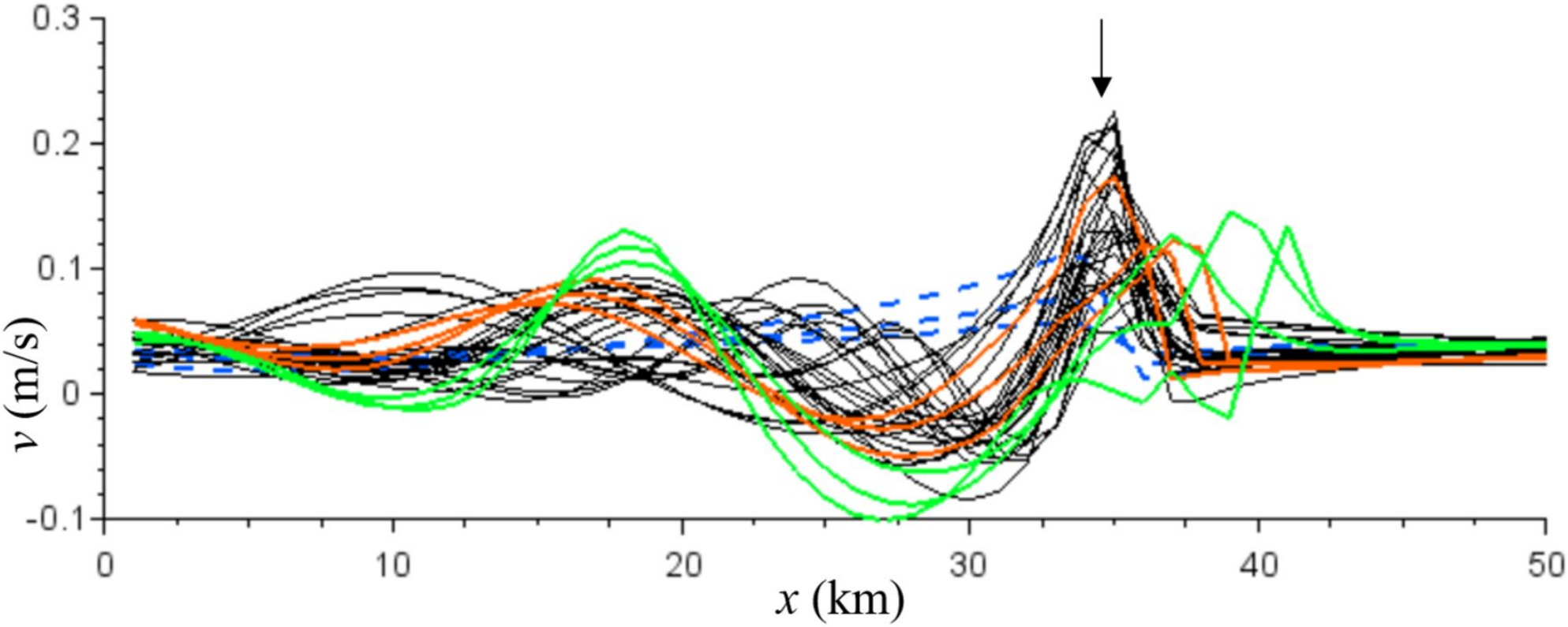
0.3
0.2
0.1
0
-0.1
v (m/s)
0
10
20
30
40
50
x (km)

Figure 14.

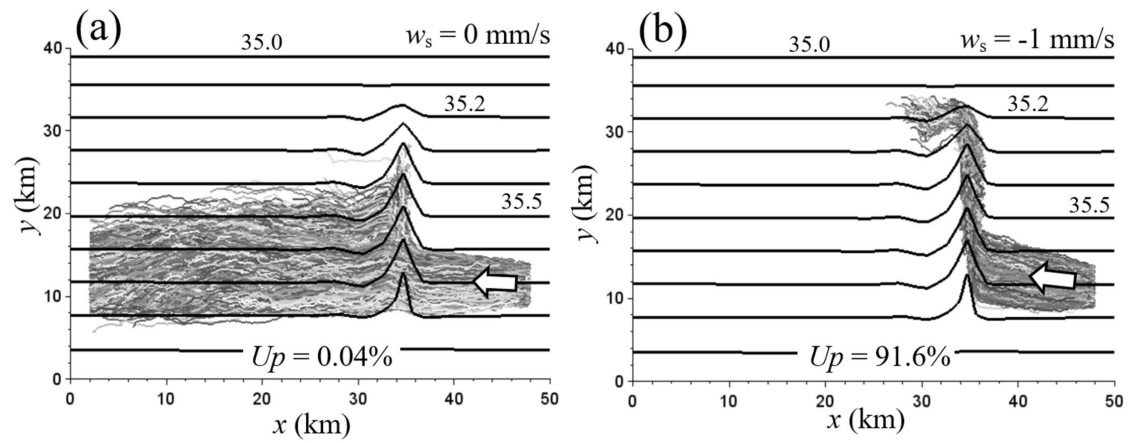
(a)
35.0
w_s = 0 mm/s
35.2
35.5
Up = 0.04%
(b)
35.0
w_s = -1 mm/s
35.2
35.5
Up = 91.6%
y (km)
x (km)
0
10
20
30
40
50

Figure 15.

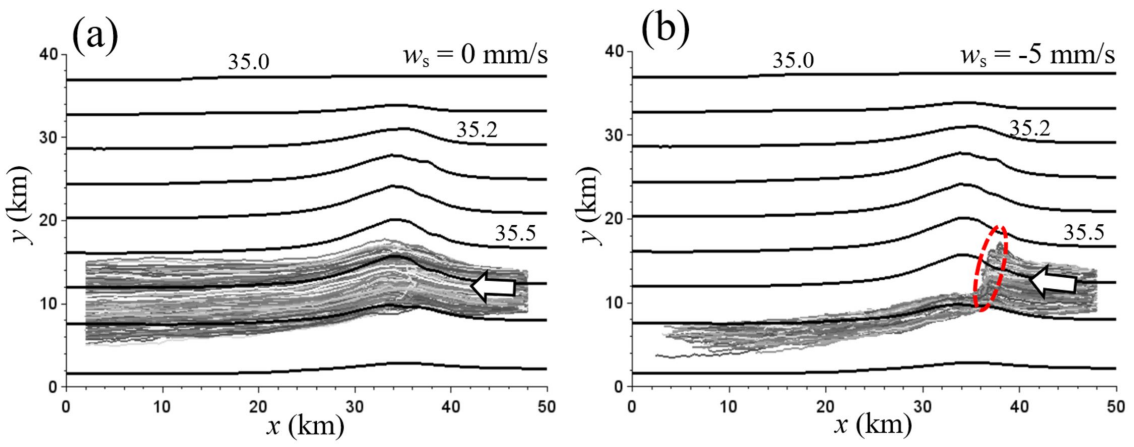
(a)
35.0
w_s = 0 mm/s
35.2
35.5
y (km)
x (km)
(b)
35.0
w_s = -5 mm/s
35.2
35.5
y (km)
x (km)

Table 1: Parameter settings and variations

Parameter	Symbol	Unit	Control value	Variations
Ambient flow speed	U	cm/s	20	5, 10
Channel width[a]	W	km	5	10
Channel depth[a]	H	m	100	0, 50, 200
Stability frequency	N	10^{-3} s^{-1}	2.17	0.86, 1.91, 3.82
Coriolis parameter	f	10^{-4} s^{-1}	-1.0	-0.8, -1.2, -1.4
Vertical eddy diffusivity	D_Z	10^{-2} m^2/s	2.0	0.02, 0.2, 0.5, 5.0
Horizontal eddy diffusivity	D_H	m^2/s	1.0	5.0, 10.0
Bed roughness length	δ	mm	2.0	0.2, 10.0
Bottom drag coefficient[b]	C_D	10^{-3}	4.3	2.3, 7.9
Ambient bottom inclination	s	m/km	25 ($\approx 1.4^o$)	17.5, 32.5 (1^o-1.9^o)

[a]Additional experiments consider U-shape and V-shape channels (see Figure 2b).

[b]Value corresponding to δ, calculated from (2).